A Search for Long-Lived Doubly-Charged Higgs Boson Production with $\bar{p}p$ Collisions at $\sqrt{s} = 1.96\ TeV$ using Run 2 CDF

by

Joshua P. Tuttle

Department of Physics
Duke University

Date:_____
Approved:

_____
Dr. Ashutosh V. Kotwal, Supervisor

_____
Dr. Alfred T. Goshaw

_____
Dr. M. Ronen Plesser

A thesis submitted in partial fulfillment of the
requirements for the degree of Master of Science
in the Department of Physics
in the Graduate School of
Duke University

2005

ABSTRACT

(Physics)

A Search for Long-Lived Doubly-Charged Higgs Boson Production with $\bar{p}p$ Collisions at $\sqrt{s} = 1.96\ TeV$ using Run 2 CDF

by

Joshua P. Tuttle

Department of Physics
Duke University

Date: _____
Approved:

_____
Dr. Ashutosh V. Kotwal, Supervisor

_____
Dr. Alfred T. Goshaw

_____
Dr. M. Ronen Plesser

An abstract of a thesis submitted in partial fulfillment of the
requirements for the degree of Master of Science
in the Department of Physics
in the Graduate School of
Duke University

2005

Abstract

We present a search for a quasi-stable doubly-charged Higgs particle at CDF using the Fermilab Tevatron for $\sqrt{s} = 1.96$ TeV. The data presented are from approximately 290 pb^{-1} of integrated luminosity collected using the upgraded Run 2 Collider Detector at Fermilab. These data were taken between February, 2002 and February, 2004. The long-lived decay products of Z's are selected in the central detector region ($|\eta| < 1.0$). We select events triggered on a muon candidate having $p_T > 18$ GeV in the event. After offline reconstruction, we require two isolated tracks ($p_T > 20$ GeV) in the event, one of which points to a stub in a muon detector. Since our search is based on the increased ionization a doubly-charged particle would produce as it passes through the detector, we require that both tracks be highly ionizing for an event to be selected as a $H^{\pm\pm}$ candidate. No such candidates are observed in the data. We set a lower mass limit of 146 GeV on a quasi-stable $H^{\pm\pm}$ boson.

Acknowledgements

I would like to express my deepest gratitude to the following individuals:

My advisor, Ashutosh Kotwal, without whom this thesis may have never even been started. His guidance in the realm of physics has been monumental, and his patience has been legendary. Whether it was in explaining to me a concept for the third time or in encouraging me to keep moving forward he was to me both a mentor and a sounding board for ideas. From that first meeting at the Thai restaurant in Batavia, I caught a glimpse of an intense passion for high-energy physics and knew that I would learn much under his tutelage.

My fellow CDF graduate students and postdocs, without whom I would have neither "learned the ropes" nor even known where to look for them. Susana Cabrera, Sebastian Carron-Montero, Heather Gerberich, Chris Hays, Dean Hidas, Yimei Huang, Mike Kirby, and Michael Mulhearn each played a critical role in some aspect of my analysis and for that I give them my sincere thanks. From learning the Duke ntuple to utilizing the compute Farms, the practical knowledge they shared was the lifeblood of this thesis.

My CDF godparents for this analysis, Amit Lath, Benjamin Brau, and Matthew Jones, without whom the finer points of the analysis may have been passed over. Between these three and the Exotics Group conveners, Beate Heinemann and Stephan Lammel, the analysis was purged of its inaccuracies and inconsistencies, resulting in a finished work that is better than it could have ever been in isolation.

All my friends from Duke, without whom I may not have been able to retain my sanity through my first and second years. This category includes but is not limited to Caroline Berger, T. Brian Bunton, Joseph Kinast, Bradley Marts, Matthew Prior,

Amanda Sabourov, Brian Tighe, and John Wambaugh. Each one provided in his or her own way an abundance of information, inspiration, and laughs. Those lunchtime debates and late-night problem sessions kept me coming back for more every day.

Others who were there along the way, without whom an unfinished thesis would still be sitting on my hard drive. Thank you to Bonnie Lilgenberg for providing a much needed final proofread of this document. Tim Tsuei, Duke Ph.D. cardholder, always pointed out that the end was in sight and reminded me that it could be a reality. The job is nice too.

My devoted family, without whom graduate school would have never been an option. Loraena, my beautiful wife and the love of my life, has been such an encouragement and steady support every step of the way. My parents played the role of both enabler and motivator from as early as I can remember. Adam and Jacquelyn always stood by me, while teaching me that being siblings does not mean being rivals.

Most importantly, my God and heavenly Father, without whom I could not even draw breath. The grace and strength that you have given me throughout this project are immeasurable. Thank you for loving me while I was unlovely, for providing hope within each day, and for the personal relationship you have provided through the gift of your Son.

To Loraena, for making it all worthwhile

Contents

List of Tables

List of Figures

Chapter 1

Introduction

> I do not know what I may appear to the world; but to myself I seem to have been only like a boy playing on the seashore, and diverting myself in now and then finding a smoother pebble or a prettier shell than ordinary, whilst the great ocean of truth lay all undiscovered before me.
> -Sir Isaac Newton

The above quotation, by a scientist much greater than I, serves to capture many of my feelings regarding scientific discovery. I am convinced that while mankind has progressed admirably in efforts to understand the universe we inhabit, we have merely scratched the surface of all that is out there to uncover and understand. The relatively young field of high-energy experimental particle physics is not immune to this limited grasp of the nuances of the universe. In fact, while many great discoveries have been made in the past fifty years, we still have a great deal to learn about the properties, interactions, and even existence of many fundamental particles. This results in a nearly limitless supply of interesting experiments and searches to undertake, which is great news for the experimentalists among us.

I am convinced that there are many good reasons to perform a search for an exotic particle. A discovery would potentially give us a better understanding of the universe, all while serving to debunk the theories which we hold so dear. To provide

a relevant example, if the long-lived doubly-charged Higgs boson were definitively proven to exist then the current Standard Model would no longer accurately describe the world of physics. It woud still provide a reasonable approximation in many cases, but a newer, more complete theory would step in to fill its place of prominence. In stark reality, we would be forced to realize that the Standard Model never provided a truly accurate representation of the physical laws which govern.

Since scientific theories are imagined by men and women capable of error, and are supported by experimentation potentially fraught with mistakes, this incomplete knowledge is and will always be the state of science in general and physics specifically. Definitive truth about the composition and nature of the fundamental pieces of our universe may be grasped for, but can never be obtained. Each discovery leads to more complete information and another piece in the puzzle, but unfortunately it becomes apparent that this puzzle will never be completed. The generation of additional knowledge through scientific experimentation can serve as both friend and foe to the scientist. It provides both a sense of fulfillment from being able to add to the overall picture and one of inadequacy from being unable to bring it to completion. Such, in my mind, is the beauty and mystery of high-energy physics.

Chapter 2

Theory

The field of high energy physics is a relatively young one. Its youth tends to make it all the more exciting though, as novel theories are written and groundbreaking discoveries are made almost daily.

From the days of Democritus around the fifth century B.C., natural philosophers have tried to determine the fundamental makeup of the universe around us. Performing the work of early physicists, these philosophers had few methods of experimentation, yet they still made some very astute observations about the atomic nature of matter. The observations began to be tested in the late nineteenth century with the advent of cathode ray tubes and precision measurement tools. Using this new technology, J.J. Thomson discovered the electron and made an early attempt to incorporate this particle into the atom's structure. Not long after, Ernest Rutherford performed experiments with gold foil and concluded that the atom has a very small positively charged nucleus. These early forays into the internal workings of the atom were only scratching the surface of the work that would follow in the next 100 years.

High energy physics has taken these early building blocks and divided them even further. Our current understanding of the composition of matter, and how it interacts with other matter is encapsulated in a theory called the Standard Model.

2.1 The Standard Model

During the decades immediately following the Second World War, the experimental particle physics community experienced a great flurry of activity. Using bubble chambers to track previously invisible particles, scientists were regularly able to make new particle discoveries. They were without an adequate theory with which to explain many of these new states, and out of this void the Standard Model was born. It was during the late 1970's that the Standard Model underwent its greatest evolution and gained most of its current form.

2.1.1 Particles

The Standard Model describes the universe in which we live by describing the fundamental constituents and forces of matter. The fermions are the smallest known constituents of matter, existing as spin-$\frac{1}{2}$ particles in two species known as quarks and leptons. Each species can be further divided into three generations of doublets, as shown in Table 2.1.

Fermionic Family	1st Generation	2nd Generation	3rd Generation
Quarks	up, down	charm, strange	top, bottom
Leptons	electron, ν_e	muon, ν_μ	tau, ν_τ

Table 2.1: The three generations of fermions.

Quarks possess the unique quality of never being found isolated in nature. They exist in bound states with other quarks in objects known as hadrons. Since quarks are spin-$\frac{1}{2}$ they obey Fermi-Dirac statistics and can only exist in two spin states.

They carry fractional electric charge in units of 1/3 or 2/3 the proton's charge, as can be seen in Table 2.2.

Quark	Mass	Charge	Spin	Antiparticle
u	1.5 - 4.0 MeV/c^2	2/3	1/2	$\bar{u}$
d	4 - 8 MeV/c^2	-1/3	1/2	$\bar{d}$
c	1.15 - 1.35 MeV/c^2	2/3	1/2	$\bar{c}$
s	80 - 130 MeV/c^2	-1/3	1/2	$\bar{s}$
t	174.3 $\pm$ 5.1 GeV/c^2	2/3	1/2	$\bar{t}$
b	4.1 - 4.4 GeV/c^2	-1/3	1/2	$\bar{b}$

Table 2.2: The basic quark properties.

Leptons have the interesting characteristic of being completely uninfluenced by the strong force. These particles are indivisible and also obey Fermi-Dirac statistics due to their half-spin. They make up a combination of three relatively heavy, charged particles and three nearly massless, electrically neutral particles. The properties and the associated antiparticles can all be seen in Table 2.3.

Lepton	Mass	Charge	Spin	Antiparticle
e^-	0.511 MeV/c^2	-1	1/2	e^+
μ^-	105.66 MeV/c^2	-1	1/2	μ^+
τ^-	1776.99 MeV/c^2	-1	1/2	τ^+
ν_e	< 3 eV/c^2	0	1/2	$\overline{\nu_e}$
ν_μ	< 0.19 MeV/c^2	0	1/2	$\overline{\nu_\mu}$
ν_τ	< 18.2 MeV/c^2	0	1/2	$\overline{\nu_\tau}$

Table 2.3: The basic lepton properties.

2.1.2 Forces

These quarks and leptons interact with each other through the exchange of force-mediating bosons. The Standard Model describes three forces: strong, weak, and electromagnetic. Virtually all tests of the Standard Model's predictions of these forces have confirmed its validity. The gravitational force, while not currently incorporated in the Standard Model, is often included with the other three fundamental forces, so we show its properties as well in the summary located in Table 2.4.

Interaction	Mediator	Coupling Constant (Mc^2 = GeV)	Range (m)	Typical Lifetime (s)
Strong force	g	< 1	$\leq 10^{-15}$	10^{-23}
Electromagnetism	γ	1/137	∞	10^{-20}
Weak force	$W^{\pm}, Z^0$	10^{-6}	10^{-18}	10^{-10}
Gravitation	graviton	10^{-40}	∞	-

Table 2.4: The fundamental forces are listed with their associated properties. The typical lifetime gives an idea of the amount of time it would take an unstable particle to decay via that fundamental interaction.

In order to best determine which theories beyond the Standard Model are most likely to accurately describe the universe, we must analyze where the Standard Model has either failed or could do better. While the Standard Model can accurately describe the behavior of most known particles and the forces they use to interact with each other, it has recently erred in one rather large prediction. According to the Standard Model, the chargeless leptons called neutrinos have no mass. This is a position which has been shown through experimentation to be patently false.

2.2 Left-Right Symmetric Models

The Left-Right Symmetric Models are a class of potential candidates for a re-

placement to the Standard Model. Since, in the Standard Model, the only coupling via the weak interaction is to left-handed particles, neutrinos are forced to be massless. One of the key features of Left-Right Symmetric Models is that, contrary to the Standard Model's prediction, these models assume that the neutrinos possess mass. This prediction was validated in several recent experiments that demonstrated neutrino oscillations [6], which can be directly linked to their being massive particles.

The introduction of right-handed weak interactions is a major component of the Left-Right Symmetric Models. This is based on the expectation of a $SU(2)_L$ x $SU(2)4_R$ x $U(1)_{B-L}$ gauge symmetry which is spontaneously broken [7], resulting in the Standard Model's pure left-handed $SU(2)_L$ x $U(1)_Y$. The additional symmetry of these Models is (B-L) symmetry, where B and L are baryon number and lepton number respectively. Based on spontaneous parity nonconservation, it can be shown that a seesaw mechanism gives [7]

$$m_{\nu_\ell} \simeq \frac{m_\ell^2}{g m_{W_R}}. \tag{2.1}$$

This relationship between the right-handed gauge bosons and neutrino masses leads to upper limits on the latter that are very reasonable. Another interesting aspect to point out is that the leptonic mass plays a role in detemining the rate of mixing between the left and right-handed particles.

A triplet of Higgs fields is a natural consequence of electroweak symmetry breaking in the Left-Right Symmetric Models [8], which allows for both singly and doubly charged Higgs bosons.

2.3 Supersymmetric Models

One of the criteria that would allow for light $H^{\pm\pm}$ is the addition of supersymmetry to the Left-Right Symmetric Models [9,10]. Through the fermion-boson duality introduced by supersymmetry, each fermion predicted by the Standard Model acquires a supersymmetric boson partner and each boson gets a supersymmetric fermion partner. These supersymmetric models are motivated by high-energy gauge unification and string theory, and make the prediction of a $H^{\pm\pm}$ mass dependent on the right handed gauge bosons and the Planck mass according to

$$m_{H^{\pm\pm}} \sim \frac{m_R^2}{m_{Planck}}. \tag{2.2}$$

Such a light triplet motivates our search for a $H^{\pm\pm}$ in a mass range attainable with Tevatron energies ($m_{H^{\pm\pm}} \sim 0(100$ GeV).

Chapter 3

The Experiment

The Fermi National Accelerator Laboratory (FNAL) is one of the world's most renowned research laboratories. Located about 35 miles west of Chicago, Illinois, the lab exists to study the most fundamental of forces and particles while pushing technology to its extreme limit. Dozens of experiments running the gamut from particle physics to astrophysics are underway there, executed by more than 2200 scientists from over 20 countries. Fermilab, as it is often called, has pushed itself to the forefront of the high energy world, resulting in numerous innovations in detector and accelerator technology and the discovery of both the top and bottom quarks. Using the Fermilab Tevatron, the world's most powerful accelerator since 1987, the elusive Higgs boson may be discovered there at any time.

During its period of operations from 1985 to 1996, the 6.28 km circumference Tevatron accelerated protons and anti-protons to a center of mass energy of 1.80 TeV. Trillions of these high energy collisions had taken place in the general purpose Collider Detector at Fermilab (CDF) by the end of Run I (1992-1996). The result of these years of data-taking was more than 100 published papers covering the entire range of hadron collider physics.

In 1996 the Tevatron underwent technical upgrades to increase both the center of mass energy and the number of high energy events. The new center of mass energy

for this period of activity (Run II) is 1.96 TeV. To take advantage of the higher collision rate and to maximize the physics capabilities of CDF, most of the existing detector was either upgraded or replaced. This analysis uses data taken during Run II of accelerator and detector operations. We will describe the components of the upgraded detector which apply directly to this search for doubly-charged particles.

3.1 The Accelerator

The Tevatron accelerator is one of a class of synchrotron accelerators, relying on RF electric fields to accelerate the charged particles through both dipole and quadrupole magnetic fields to keep them in a tight circular orbit. Both protons and antiprotons are accelerated in opposite directions to energies of 980 GeV, but it takes many separate components to reach those energies. Figure 3.1 shows a schematic drawing of the entire accelerator chain. Each component used in accelerating the protons and antiprotons will now be described in some detail.

The high energy collision particles must begin somewhere, and at Fermilab they begin in the Cockcroft-Walton preaccelerator as hydrogen gas. Here the gas is ionized to form individual protons, each having an electron pair. An electrostatic accelerator raises the energy of these negatively charged ions to 750 keV. The second step for these ions is the Linac, a linear accelerator over one and one half football fields long using oscillating electric fields. By the time these H^- ions reach the far end of the Linac, their energy has been increased to 400 MeV, and they are ready to become pure protons. The electrons are here stripped from the protons by passing these energetic ions through a carbon foil.

Now that the protons are nearly one half GeV in energy, they are ready to enter

the Booster, a synchrotron 150 meters in diameter. The Booster is used both for raising the particle's energy to 8 GeV and for gathering the scattered protons into bunches consisting of approximately 6×10^{10} particles each.

Protons now pass from the small Booster ring to the larger ring of the Main Injector, where they reach energies of 150 GeV. The Main Injector is 3 km in circumference, having been built primarily to increase antiproton efficiency from Run I levels. Antiprotons are produced here by selecting protons that have attained energies of 120 GeV to strike a nickel target. Antiprotons, among other collision products, are collected and focused through lenses made of lithium and a magnetic field. The antiprotons proceed to the Debuncher, an accumulator ring that is used to decrease the momentum distribution through stochastic cooling. This process also makes a continuous beam out of the antiprotons by increasing spatial distribution. Next, the Accumulator cools them further and stacks them into bunches. After being accelerated to 150 GeV with the protons, they are sent to the Tevatron for final acceleration and collision. When all is said and done, the Main Injector raises the number of available antiprotons per store by a factor of 10. A luminosity increase is also achieved in the same tunnel through use of the Recycler, which saves antiprotons not utilized by the Tevatron for the next store.

When the protons and antiprotons are "shot" into the Tevatron, they have energies of 150 GeV and travel in opposite directions around this large ring. This largest of synchrotron accelerators produces particles of 0.98 TeV in bunches that cross every 396 ns on average. This means as many as 3 million beam crossings can occur each second at one of the two interaction points: B0 and D0. Particles of this energy require powerful magnetic fields to maintain their circular path, which are generated using large dipole electromagnets.

The CDFII detector, which will be discussed next, is centered around the B0 interaction point. Within the detector there is a luminous region of roughly 30 cm in the beam direction. The beam possesses a roughly circular profile, which is achieved through a series of quadrupole magnets. The dispersion of the beam is a Gaussian whose sigma is only 30 micron wide. Such a highly focused beam, if properly aimed and aligned, results in much higher luminosity in the detector.

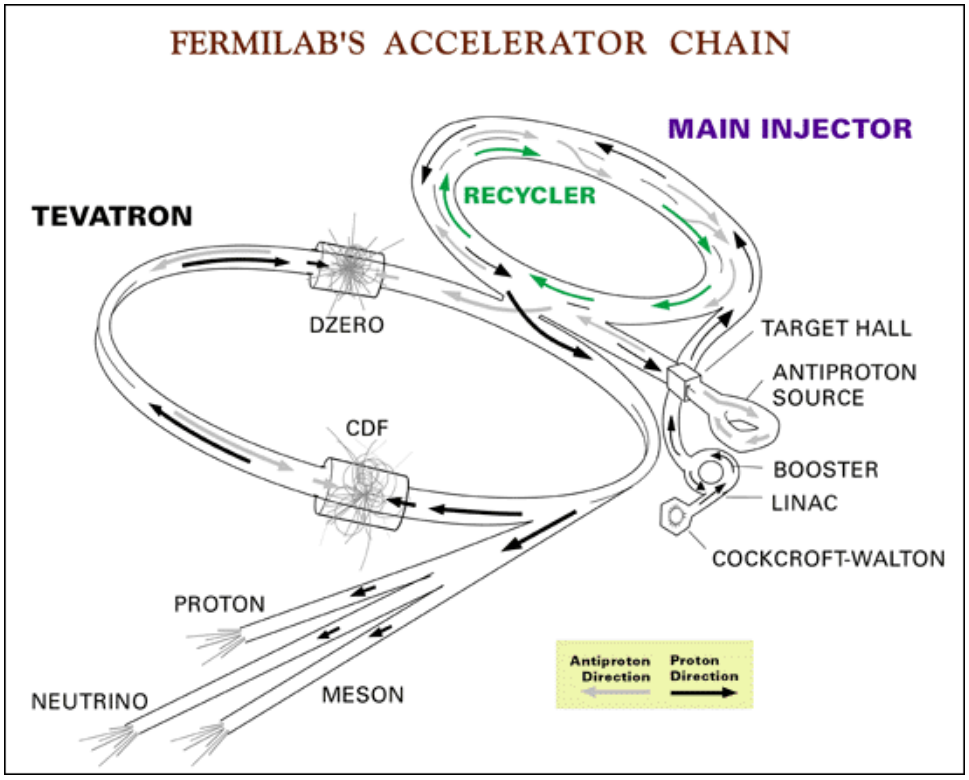

Figure 3.1: The Fermilab Tevatron used in generating proton-antiproton collisions. The label "ANTIPROTON SOURCE" indicates the location of both the Debuncher and Accumulator.

3.2 The Collider Detector at Fermilab (CDF)

3.2.1 Overview

The Run 2 Collider Detector at Fermilab (CDFII) is a cylindrically-symmetric, general purpose particle detector. Its construction is centered around a superconducting solenoidal magnet. A three-dimensional rendering of the detector can be seen in Figure 3.2. Another perspective, which introduces a human figure to show a degree of scale, can be seen in the elevation view of Figure 3.3.

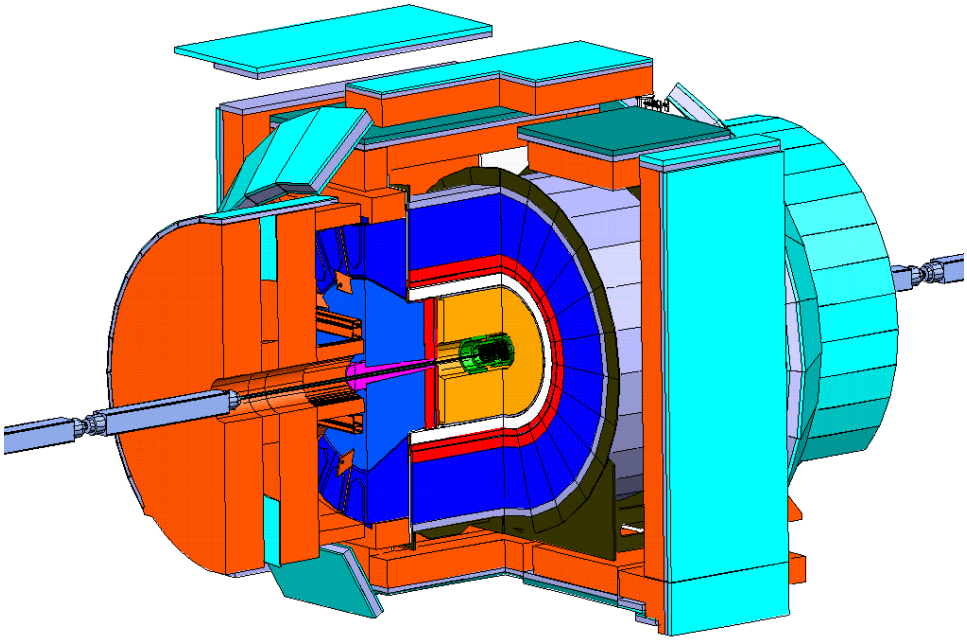

Figure 3.2: The Run 2 Collider Detector at Fermilab viewed isometrically with one quarter removed in order to reveal the tracking volume.

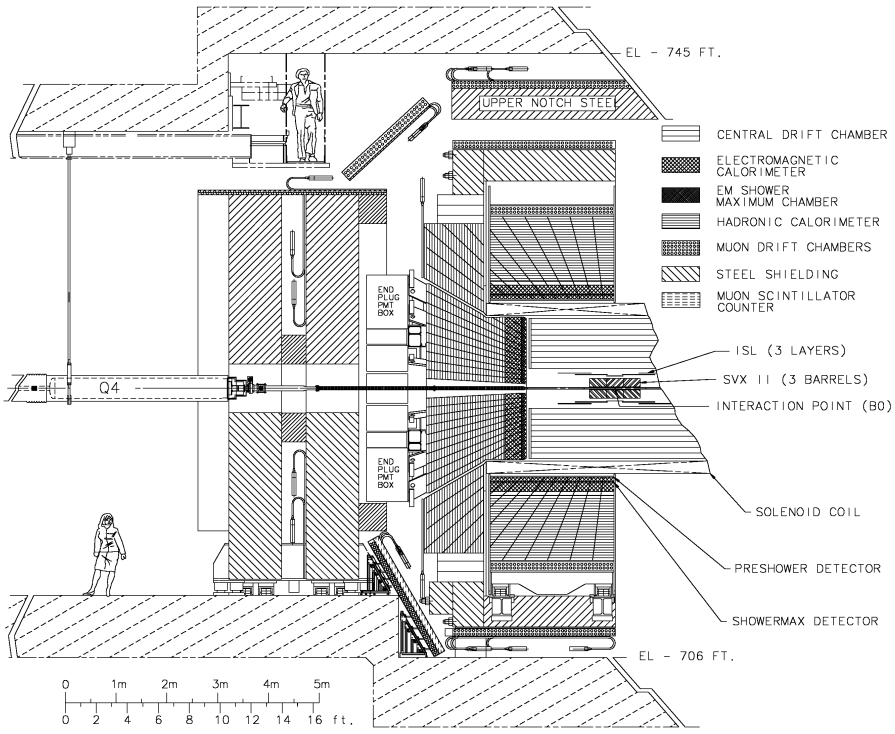

Figure 3.3: An elevation view of Run 2 CDF.

3.2.2 Coordinate System

To facilitate the understanding of terminology in the detector section, a proper definition of the CDF coordinate system must be given. CDF is oriented cylindrically, a fact which drives the cylindrical coordinate system used. This coordinate system can be seen in Figure 3.4. The z-axis is oriented along the nominal beam direction, in the same direction as the incoming protons. Its origin is at the center of the CDF detector. The azimuthal angle ϕ and the distance r are measured in the plane orthogonal to this direction (ϕ being measured in an anti-clockwise direction from the perspective of the incoming protons). θ is measured upwards from the positive z-axis, being related to z and r by the expression

$$z = r \times cos(\theta) \tag{3.1}$$

Another quantity we will use frequently is the pseudorapidity, η, which is defined as

$$\eta = -log(tan\Big(\frac{\theta}{2}\Big)), \tag{3.2}$$

and depends uniquely on the angle θ.

In addition to the cylindrical system defined above, a Cartesian coordinate system is also defined with the x and y axes oriented horizontally away from the center of ring and upward respectively. The result is a right-handed system with the z-axis remaining as previously defined in the cylindrical section above.

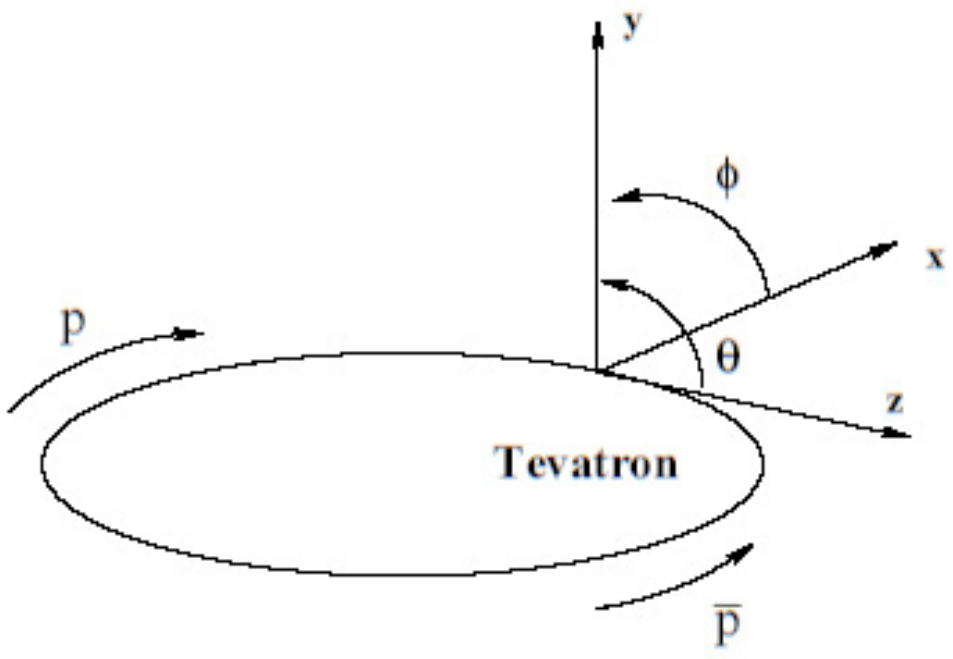

Figure 3.4: The coordinate system used at CDFII.

3.2.3 Tracking System

The integrated tracking system at CDFII involves a new open cell drift chamber, the Central Outer Tracker (COT) which covers the central region $|\eta| < 1$ and the "silicon inner tracker" system providing coverage to $|\eta| < 2$. Our analysis uses the COT exclusively for all our tracking needs, thus we do not consider forward tracks. The longitudinal view of the detectors shown in Figure 3.3 illustrates the large coverage of the COT near the detector center.

The tracking chambers are centered within a 3 m long 5 m diameter superconducting solenoidal magnetic coil, producing a uniform 1.4 T magnetic field oriented along the proton beam direction. The result of this field is an imposed curvature on the tracks of all charged particles passing through the detector. The radius of these curves can be used to directly determine the particle's momentum (assuming the particles only possess one unit of charge). The equation for determining transverse momentum (p_T) using this method for a magnetic field strength given by B is:

$$p_T = Bqr. \tag{3.3}$$

The Central Outer Tracker (COT) is a drift chamber comprised of 96 layers divided into eight superlayers, seen in Figure 3.5. These layers are placed between 40 and 132 cm from the beam pipe. Each superlayer contains 12 sense wires which alternate with potential wires in a plane. The COT is a 320 cm long cylinder, which gives the detector full coverage in ϕ. An equal mix of ethane and argon fills the drift chamber for purposes of ensuring a high drift velocity. Four of the superlayers are axial (to measure in the transverse plane) and four are stereo (to measure z) in an alternating pattern beginning with a stereo layer.

A charged particle passing through the COT leaves a trail of ions which are

collected on the sense wires, giving the r-ϕ information on the position of the hits. The three-dimensional sequence of hits is reconstructed to form a track, from which the momentum is determined based on the curvature from the magnetic field. The COT also retains information about the width of the pulse, which can be used to derive information on the ionization of the transit particle.

The track as measured by the COT defines a few variables which must be understood:

- c is the speed of light in a vacuum,
- z_0 is the position of the track vertex in the z direction,
- d_0 is the distance measured from the track vertex to the z-axis in the transverse direction (it also goes by the name "impact parameter"),
- $cot(\theta)$ is the position of the track vertex as determined by the cotangent of the polar angle θ, measured out of the plane of the Tevatron ring (useful since θ goes to zero for hard collisions and $\Delta\theta$ is nearly zero for two tracks leaving the detector in opposite directions),
- ϕ_0 is the position of the track vertex in the radial direction as seen by the beam.

3.2.4 Time of Flight System

One new feature that was added during the CDF Run II upgrade is the Time of Flight (TOF) system. It is useful in helping to identify low transverse momentum kaons and pions. The detector is a combination of 216 scintillating bars that measure the time difference between the arrival time at its location just outside the tracking

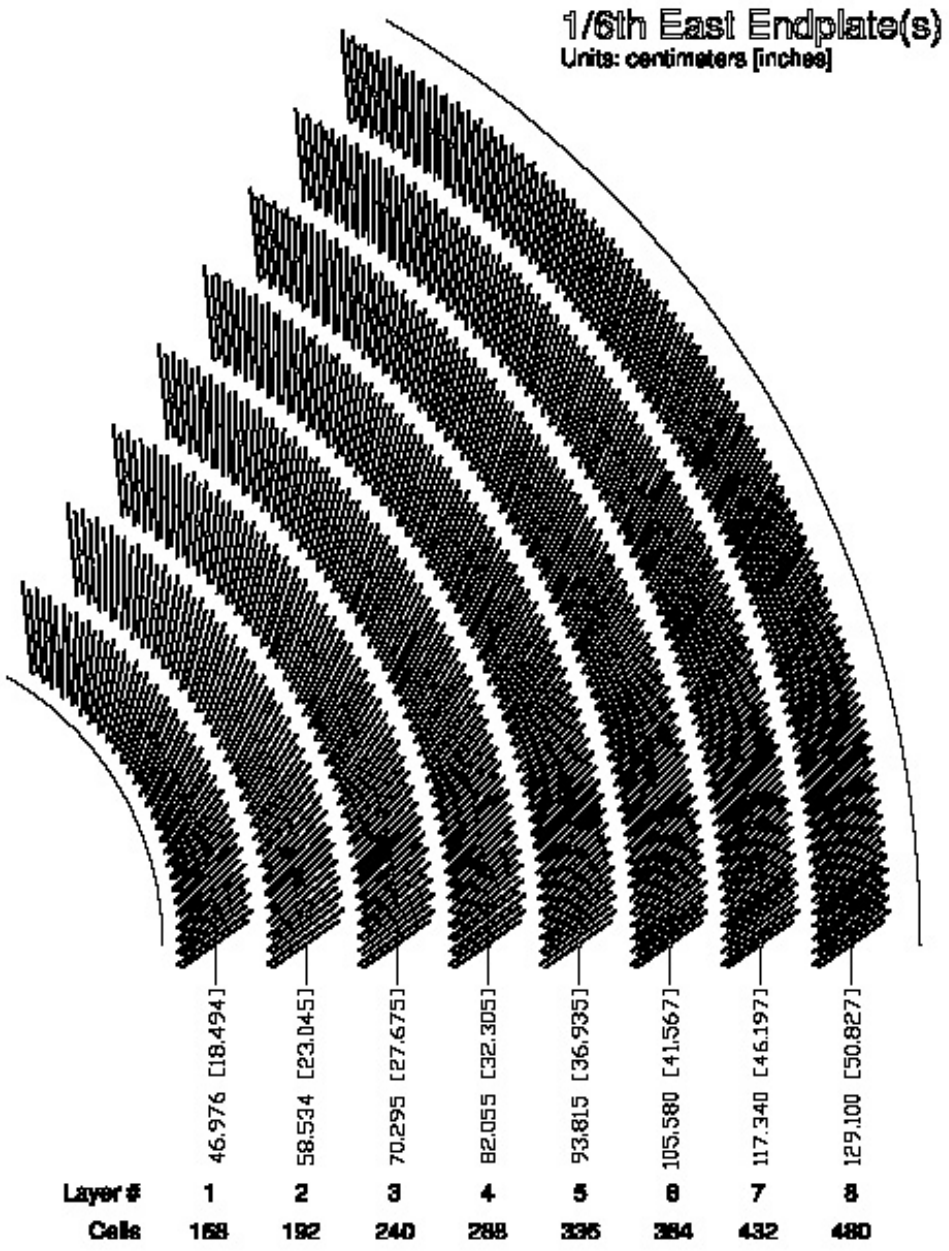

Figure 3.5: The COT is made up of eight superlayers. One-sixth of the east endplate is shown here, and for each superlayer is shown the number of supercells and the average radius.

volume and the collision time (t_0). The measurement is made with a resolution of 100 ps. This flight time information t, when coupled with the particle's momentum p and path length L, is all that is required in making a mass determination:

$$m = \frac{p}{c}\sqrt{\left(\frac{ct}{L}\right)^2 - 1}, \tag{3.4}$$

where p and L are measured by the tracking system. Our analysis, focusing on high transverse momentum particles, does not use the time of flight information measured in the TOF system.

3.2.5 Calorimeters

The next detector component reached by the high-energy collision products is the calorimetry system at CDF. Located immediately outside the solenoid, it exists to measure the energy deposited by jets, photons, and electrons produced in the $\bar{p}p$ collisions. In addition, the position can be determined roughly due to the segmentation of the calorimeter. Each of the two physically distinct sections, the Central calorimeter from Run I ($|\eta| < 1$) and the newer Plug calorimeter built for Run II ($1.1 < |\eta| < 3.64$), has both electromagnetic and hadronic portions. There is also a third end wall calorimeter spanning the gap between the central and plug calorimeters.

The calorimeters are composed of alternating layers of heavy metal and scintillating material. The metal layers force the jets, photons, and electrons to lose energy through showering. These showers are picked up by the scintillators, producing photons. After being channeled through light guides, the photons are detected by photomultiplier tubes that give an intensity. From the interaction point, the electromagnetic calorimeters are traversed first and are most sensitive to electrons

and photons losing most of their energy there. Jets deposit only a small amount of energy in these electromagnetic calorimeters, and thus carry most of their energy to the hadronic calorimeters where they shower.

The calorimeters are a large part of the CDFII detector, but since muon-like particles do not typically deposit much energy in them, it could be assumed that they will not be useful in our search. Yet, it is important to be reminded that in our study of doubly-charged particles the additional charge of an $H^{\pm\pm}$ will result in greatly increased ionization. This permits us to use the energy deposition in the electromagnetic and hadronic calorimeters as an additional discriminator for finding a highly-ionizing particle.

3.2.6 Muon Chambers

The CDF muon system forms an outer shell around all the other subdetectors. Electrons and jets deposit most of their energy in the calorimetry system, but muons from Z^0 decay leave only about $\frac{1}{2}$ GeV in the electromagnetic portion and 2 GeV in the hadronic, on average. Since very little muonic energy is deposited in the calorimeters, additional measurements are needed aside from their track information. The muon chambers fill this role admirably, composed of drift chambers and scintillating material. The Run II detector has four muon subsystems which cover the pseudorapidity range $|\eta| \leq 2.0$. They are the Central Muon detector (CMU), Central Muon Extension (CMX), Central Muon Upgrade (CMP), and Barrel Muon detector (BMU). Each subdetector is made up of layers of single wire drift chambers that allow the creation of a muon object when hits in the chamber match with a COT track, forming a "stub."

Since the analysis focuses on long-lived particles, the muon detectors are a cen-

tral component in our $H^{\pm\pm}$ search. When selecting events to include in our search, we thus require events having a stub in at least one of the muon detectors.

3.2.7 Triggers

With the excessive rate at which high-energy collisions take place at CDFII, there is no way that all events could be written to tape for analysis. Most of these collisions hold nothing of interest for scientists anyway, so a complex method was devised to rapidly determine whether an event is worth keeping or not. The result is a three-level trigger system governed by the principle that each level do its part to decrease the rate of events while eliminating deadtime. These triggers serve to reduce the event storage rate down to roughly 75 Hz from the beam crossing rate of 2.5 MHz by eliminating most of the "minimum bias" events, a reduction by a factor of 100,000.

The most primitive level of trigger selection, Level-1 (L1), is a purely hardware-based decision. Each of the subdetectors (calorimeters, muon, and tracking systems) contains a data pipeline in parallel synchronous streams. This trigger must select interesting events in the time it takes the data to reach the other end of the pipeline. The data is synchronized to the beam crossing rate of 396 ns in such a way that the L1 trigger only has about 5 μs to make the decision to keep or drop an event. Custom designed electronics select physics objects independently for each stream based on energy deposition in the calorimeter, stubs in the muon chambers, and early track reconstruction performed by the eXtremely Fast Tracker (XFT). A typical Level-1 accept rate is roughly 12 kHz, although the hardware is capable of reaching 20 kHz.

The Level-2 (L2) hardware is comprised of four buffers which are written to after

a L1 accept. When one of these buffers is processing an event it cannot be used for more L1 accepts. If all the buffers are full, deadtime may result since the buffer can accept no more events from Level-1. Decisions in L2 are based on a limited event reconstruction using higher precision than the L1 decision. Additionally, information from the shower max and SVXII systems are included, which allows for improved identification of particles and reconstruction of secondary vertices. Level-2 also enjoys the inclusion of a specific jet reconstruction algorithm. After performing reconstruction, the trigger must check whether the event passes any of the predetermined L2 criteria while maintaining an event rate below the Level-2 maximum rate of 300 Hz.

A farm of over 200 dual-processor personal computers running Linux and an Event Builder (EVB) comprise the software-based Level-3 (L3) trigger. Now that the event rate has been decreased by the L1 and L2 triggers, the EVB has sufficient time to rebuild the complete event into a single data block for the final decision. The Level-3 trigger determines whether an event can be placed into long-term storage for later analysis or must be deleted from memory forever. A bunch counter is used to ensure that digital information from each subdetector combines for the same bunch crossing only. All L1 and L2 data is resident only on a readout crate, but at the L3 trigger, everything for the event is reconstructed and analyzed at once on a processor. This trigger is also made aware of calibration information, due to more available processing time. The only limiting factor for the L3 accept rate is the rate at which events can be written to tape, which is roughly 75 Hz. Once the data is placed on tape storage, it is ready for offline reconstruction and analysis.

Chapter 4

Event Selection

Now that the setup of detectors used by the analysis has been explained, it is befitting to describe the selection methods employed in the search. The three trigger levels we select for our analysis eliminate low momentum particles and events without stubs in the muon chambers. The events that remain after the selection of the Level-3 trigger are reconstructed offline and completely calibrated for slight detector variance. Selection cuts are defined on these events, choosing only events with a pair of isolated high p_T particles having enhanced ionization. Only high quality tracks can be used in a search, so each track must consist of a certain number of "hits" and pass through a preferred region of the detector. The remainder of this chapter quantifies and expands upon these selection cuts used for identifying doubly-charged candidate particles.

4.1 Triggers and Dataset

4.1.1 Trigger Paths

The dataset used for this analysis is collected using the MUON_CMUP_18 and MUON_CMX_18 trigger paths (Table 4.1).

Trigger	Level	Track Cut(s)	Muon Cut(s)
MUON_CMUP_18	1	$p_T > 6$ GeV	CMU stub, > 2 CMP layers
	2	$p_T > 8$ GeV	none
	3	$p_T > 18$ GeV	CMU $\|\Delta x\| < 20$ cm
			CMP $\|\Delta x\| < 10$ cm
MUON_CMX_18	1	$p_T > 8$ GeV	CMX stub
	2	none	none
	3	$p_T > 18$ GeV	CMX $\|\Delta x\| < 10$ cm

Table 4.1: The requirements for the triggers in our analysis.

4.1.2 Dataset

The $\sim 290\ pb^{-1}$ of data were collected between February, 2002 and February, 2004. The datasets that the signal sample is taken from were `bhmu08` and `bhmu09`. The sample was separated into runs having both the CMUP and CMX, runs having the CMUP only, and runs having the CMX only. The good run lists used were compiled by Chris Hays [15] using the CDF e-logs and the COT and calorimeter good run lists. After selecting only the good runs, we analyzed $(250.9 \pm 14.3)\ pb^{-1}$ of data from the runs with both CMUP and CMX, $(32.1 \pm 1.8)\ pb^{-1}$ using CMUP only, and $(9.0 \pm 0.5)\ pb^{-1}$ using the CMX only. The data were processed using CdfSoftware version 5.3.1 production processing.

4.2 Ionization

Massive charged particles traveling post-collision through the CDF detector primarily lose energy due to ionization. The ionization produced by these particles is given by the Bethe-Bloch equation [11]:

$$-\frac{dE}{dx} = Kz^2\frac{Z}{A}\frac{1}{\beta^2}[\frac{1}{2}\ln(\frac{2m_e c^2\beta^2\gamma^2 T_{max}}{I^2}) - \beta^2 - \frac{\delta}{2}], \tag{4.1}$$

where K is a constant for all materials, z is the charge of the incident particle, Z and A are the atomic number and atomic mass of the absorber respectively, β is the relativistic factor $\frac{v}{c}$, m_e is the electron mass, c is the speed of light in vacuum, γ is the relativistic factor given by $(1-\beta^2)^{-\frac{1}{2}}$, T_{max} is the largest kinetic energy a free electron can receive during a collision, I is the mean excitation energy, and δ is a correction due to the density effect.

Since the ionization of a particle is proportional to the square of its charge, a doubly-charged particle would cause four times the ionization of a singly-charged one. We exploit this large difference in ionization in our search for a long-lived doubly-charged Higgs.

4.2.1 Measurement of Ionization

Energy loss due to ionization can be measured several different ways within the CDF detector. We employ the combined dE/dx measurements of calorimeters and tracking devices to get a complete picture of a particle's ionization.

Both the hadronic and electromagnetic calorimeters measure dE/dx for minimum-ionizing particles. We use the transverse component of these energy-depositions as recorded by each calorimeter along the track of the particle whose ionization we seek to measure. We call these quantities $HadET$ and $EMET$ respectively.

The COT also encodes dE/dx information in the width of the pulse of each hit, and provides a particularly useful ionization measurement. In this analysis we use the COT dE/dx measurement calibrated at the hit-level by Eiko Yu *et.al* [12] and at the "macroscopic" run-level by members of the CDF bottom group [13] which we denote by the abbreviation $COTHW$.

4.2.2 Detector Mismeasurement of Ionization

Whether or not a particle can be considered highly ionizing based on its $HadET$, $EMET$, and $COTHW$ values is subject to detector effects. There are several detector and event characteristics that can contribute to mismeasurement of these variables and thus allow a generic particle like a muon to occasionally mimic a highly ionizing particle.

It is statistically possible for a muon to occasionally give large values for each of the three measured dE/dx quantities. Other particles in close proximity to a muon can increase the apparent ionization produced by the muon. Thus, it is advantageous to use a combination of all three variables to eliminate many of these anomalous readings, thereby reducing the rate of muons mimicking highly ionizing particles.

In events with a large number of tracks or tracks very close together, real muon hits can become merged with other nearby hits thus increasing the pulse width recorded by $COTHW$. Studies of fake rate systematics in Section 6.1.2 illustrate the increase in fake highly ionizing muon events measured by $COTHW$ as the number of tracks in the COT increases.

The calorimeter can experience mismeasurement of $HadET$ and $EMET$ when underlying event or jet energy overlaps the muon towers being analyzed. Such an overlap could also allow the muon to be mislabeled as a highly ionizing particle.

4.3 Selection Criteria

There are three tables defining our cuts in this analysis. Table 4.2 gives both the Track Cuts and Stub Cuts referenced throughout, Table 4.3 gives the muon ID

cuts which we use for counting the number of $Z \rightarrow \mu\mu$ events in the current data sample, and Table 4.4 gives the cuts we use for identification of a $H^{\pm\pm}$.

Variable	Cut
Track Cuts:	
$\|z_0\|$	< 60.0 cm
# Stereo hits	≥ 3 SL with ≥ 5 hits or COT layer < 96
# Axial hits	≥ 3 SL with ≥ 5 hits or COT layer < 96
$\|d_0\|$	< 0.2 cm
(isolation in R=0.4 cone)/p_T	< 0.1
p_T	> 20 GeV
ρ_{COT}	> 140 cm
Cosmic Ray Veto	
Stub Cuts:	
$\|\Delta x_{CMU}\|$	< 3.0 cm
$\|\Delta x_{CMP}\|$	< 5.0 cm
$\|\Delta x_{CMX}\|$	< 6.0 cm
Fiducial Muon	

Table 4.2: Track Cuts and Stub Cuts used throughout the analysis.

Variable	Cut
Track Cuts	from Table 4.2
Stub Cuts	from Table 4.2
E_{em}	$< 2 + \max(0,(p - 100) \times 0.0115)$ GeV
E_{had}	$< 6 + \max(0,(p - 100) \times 0.0280)$ GeV

Table 4.3: Muon ID cuts.

In addition to the tables showing the value of the cuts, some text is given here to describe the parameters being cut on:

- z_0 – The z vertex position of the high p_T track, extrapolated to the beamline.
- # Stereo/Axial hits – The number of hits deposited on the appropriate type

of COT superlayer segment by the track.

- d_0 – The impact parameter relative to the measured position of the beam. A powerful cut for reducing cosmic ray background.

- Isolation fraction – The isolation of a particle, calculated from the sum of all calorimeter energy found in a cone around the primary particle and divided by the transverse momentum of the particle. The energy assigned to that particle's track is not included in the sum.

- p_T – The transverse momentum of the track, selected as the beam constrained COT track with the highest momentum pointing to a muon stub.

- ρ_{COT} – The COT exit radius, calculated to ensure that the particle passes through all eight superlayers having high efficiency for triggering an event.

$$\rho_{COT} = \frac{\eta}{|\eta|} \times \frac{Z_{COT} - Z_0}{\tan(\lambda)} \tag{4.2}$$

where

$$\lambda = \frac{\pi}{2} - \theta. \tag{4.3}$$

- Δx_{CMU} – Track and stub matching distance in the CMU.

- Δx_{CMP} – Track and stub matching distance in the CMP.

- Δx_{CMX} – Track and stub matching distance in the CMX.

- E_{em} – Energy deposited in the central electromagnetic calorimeter (CEM).

- E_{had} – Energy deposited in the central hadronic calorimeter (CHA).

We define two separate sets of ionization cuts in our analysis. The loose cuts seek to maximize efficiency and are used exclusively for setting a mass limit. The tight cuts, on the other hand, are used to virtually eliminate the fake backgrounds and will be used only in case of discovery. Since the combined cuts on $EMET$ and $HadET$ are fairly inefficient, the ability to set the best limit suffers when using them. Thus, Table 4.4 indicates we completely removed these cuts in our loose category.

Variable	Loose Cuts	Tight Cuts
EMET	no cut	> 0.6 GeV
HadET	no cut	> 4 GeV
COTHW	> 35 ns	> 35 ns

Table 4.4: The three high ionization cuts used in identifying $H^{\pm\pm}$. We use the loose ionization cuts only for setting a limit, and the tight ionization cuts only for possible discovery of $H^{\pm\pm}$.

Variable	Cut
Highly Ionizing Track with Stub	from Tables 4.2 & 4.4
Second Highly Ionizing Track	from Tables 4.2 & 4.4

Table 4.5: $H^{\pm\pm}$ ID cuts.

Chapter 5

Signal Efficiencies and Acceptance

Two large components of any particle search are efficiency and acceptance. Together they determine whether or not the object of the search will be found if generated in a particle collision. Each are described in detail in their own respective sections.

5.1 Efficiencies

This section describes how efficiently our trigger, reconstruction, and selection cuts choose a particle or group of particles. For example, even though we may require that all muons pass a certain set of cuts, we inevitably exclude some muons that do not pass those cuts. This can be the result of measurement errors in the detector, or simply due to a long tail in a distribution that must be cut somewhere. A perfectly efficient cut is one which does not exclude any potential candidate particles. Choosing the "best" cut value requires a compromise between this cut having 100% efficiency, and one which introduces as few non-candidate particles (called background) as possible.

5.1.1 Muon ID Efficiencies

We find the efficiency to identify muons using Z data by selecting events with two opposite-sign muon candidates having a reconstructed mass between 80 and 100 GeV. We require that one of these muons must pass the Track Cuts in Table 4.2, while the second is required to pass only the p_T, $|z_0|$, and ρ_{COT} cuts in that table and a looser cut on d_0 ($|d_0| < 1$ cm) while removing identified cosmics. From the resulting sample, we count events where the second muon passes all the Track Cuts (N_2) and also events where the second muon fails the Track Cuts (N_1). From these two numbers we calculate the efficiency of the Track Cuts to be:

$$\epsilon = \frac{2N_2}{2N_2 + N_1} \tag{5.1}$$

I similarly found the Trigger and Stub efficiencies for the CMUP and CMX detectors. Chris Hays found the cosmic ray tagger to be 100% efficient, with an upper limit of 0.8% on the inefficiency [15]. Thus the cosmic tagger efficiency is considered to be $100.0^{+0.0}_{-0.8}$%. For the $|z_0|$ cut we used the efficiency given by the WZ cross section group [17].

I show this efficiency for All Track Cuts, as well as the CMUP/CMX Trigger and Stub efficiencies [15] in Table 5.1.

Selection Criteria	Efficiency (%)
$\|z_0\| < 60$ cm	95.0 ± 0.4
All Track Cuts	93.6 ± 0.2
CMUP Trigger & All Stub Cuts	78.8 ± 1.1
CMX Trigger & All Stub Cuts	94.1 ± 0.7

Table 5.1: Muon ID efficiencies.

5.1.2 Calorimeter Ionization Cut Efficiency

Efficiencies were also calculated for the calorimetry highly ionizing cuts. We counted the number of cosmics with ionization values ($EMET$ and $HadET$) quadrupled that passed each cut. These cosmics represent the doubly-charged signal events and thus they were used in calculating the signal efficiencies seen in Table 5.2.

Variable(s) cut	Cut Value	# Cosmic events (out of 216,224)	Efficiency (%)
$EMET$	> 0.6 GeV	184,321	85.25 ± 0.08
$HadET$	> 4 GeV	191,790	88.70 ± 0.07
$EMET$ & $HadET$	> 0.6 GeV, > 4 GeV	175,333	81.09 ± 0.08

Table 5.2: Calorimeter ionization cut efficiencies after cuts in Table 5.1 have been made.

5.1.3 COTHW Ionization Cut Efficiency

Since there are limitations in measuring very small pulse widths recorded by $COTHW$, the lower tail of the quadrupled $COTHW$ variable is cut off. Therefore, it would be incorrect to quote any efficiency by simply counting the number of highly ionizing ($COTHW \times 4$) cosmic events that pass the 35 ns cut. We chose to use the alternate method explained below for calculating the efficiency of this variable.

To begin, we needed to isolate a highly ionizing sample in the data that could not be part of the $H^{\pm\pm}$ signal. We used the Universal Curve predictions from [13] to draw theory curves of dE/dx vs. p_{track} for various particles, and then overlaid these curves on a scatter plot of data events. The data we use includes all positively charged tracks with ≥ 5 hits in ≥ 3 stereo superlayers and ≥ 3 axial superlayers. We also required $|d_0| \geq 1$ cm for these tracks in the data. The resulting graph

can be seen in Figure 5.1. From this plot, we chose to isolate a proton band somewhere in the momentum range of 300-600 MeV which would have roughly the same $COTHW$ spectrum as our cosmic $COTHW \times 4$ sample. We divided this momentum range into 50 MeV bins which can be seen in Figure 5.2. The rightmost peaks of the histogram correspond to a proton sample, and the curve with the highest dE/dx (300-350 MeV) is the one we will isolate for the efficiency calculation. Figure 5.3 shows this highly ionizing proton sample compared to our $COTHW \times 4$ cosmic sample. Although the proton sample is taken from a portion of the momentum curve that is slanted, our 50 MeV slice should be narrow enough to prevent any distortions or skewing of the shape. Also, since the proton sample has slightly smaller $COTHW$ values, the efficiency we derive from this sample will be an underestimate of the true $H^{\pm\pm}$ efficiency.

In order to provide a cleaner sample of protons, we want to use the equal distribution of positive and negative pions and kaons to remove these additional peaks. Figure 5.4 shows the positively charged and negatively charged distributions overlaid. Subtracting these distributions gives us a much improved proton peak in Figure 5.5. We also show the $H^{\pm\pm}$ $COTHW$ distribution as predicted by the Universal Curve. It is clear from this theoretical prediction that the proton peak in the 300-350 MeV range is the correct one to use for measuring the efficiency of the $COTHW$ cut on $H^{\pm\pm}$ particles. Table 5.3 shows the $COTHW$ efficiency we found from the pion-subtracted distribution of protons in the 300-350 MeV momentum window. Since the only inefficiency is due to kaons near our proton peak and the $H^{\pm\pm}$ Universal Curve shows no efficiency loss, we believe our 35 ns cut on $COTHW$ is fully efficient. We apply a systematic of -0.5% to cover the alleged inefficiency from the low-momentum proton distribution.

Cut Value	# Proton events (out of 93,271)	Efficiency (%)
COTHW > 35 ns	92,865	99.56 ± 0.02

Table 5.3: *COTHW* cut efficiency after cuts in Table 5.1 have been made.

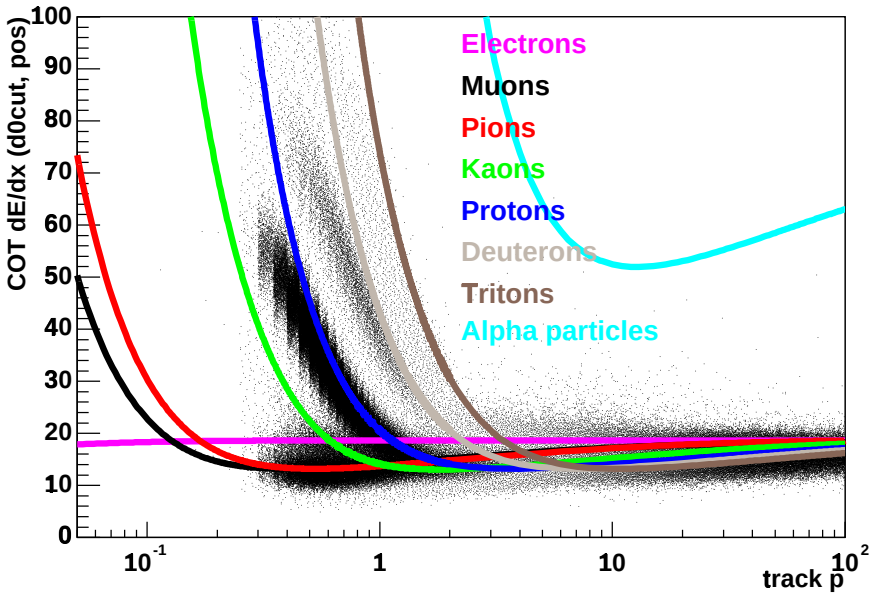

Figure 5.1: Scatter plot of all positive tracks having ≥ 5 hits in ≥ 3 stereo SL's and ≥ 3 axial SL's, as well as $|d_0| \geq 1$ cm. The overlaid lines were calculated from the B group's Universal Curve prediction.

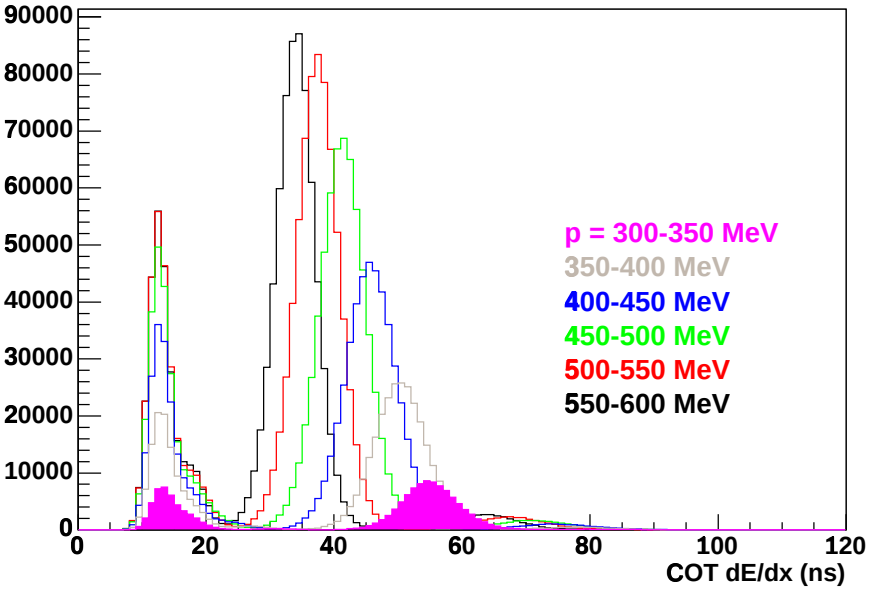

Figure 5.2: Peaks on right correspond to a highly ionizing band of protons in 50 MeV bins of the scatter plot shown in Figure 5.1.

5.1.4 $H^{\pm\pm}$ ID Efficiency

The ID efficiency of a doubly-charged Higgs event is the product of the individual muon efficiency properly applied to two particles and the efficiencies of the high ionization cuts on $EMET$, $HadET$, and $COTHW$. Table 5.4 summarizes these efficiencies.

The use of muons for measuring the efficiency of a doubly charged particle may not give an accurate measurement due to edge effects in muon towers and multiple scattering. The edge effects would potentially affect our cut on the isolation ratio of the particle. To address this and get a conservative estimate of the edge effects involved, we calculated what percentage of the muon tower's area is within 0.5 cm of the edge of the tower. Each tower subtends an angle of 0.1 radians in η and 0.25 radians in ϕ, so if we estimate the calorimeter surface lies 2 meters from

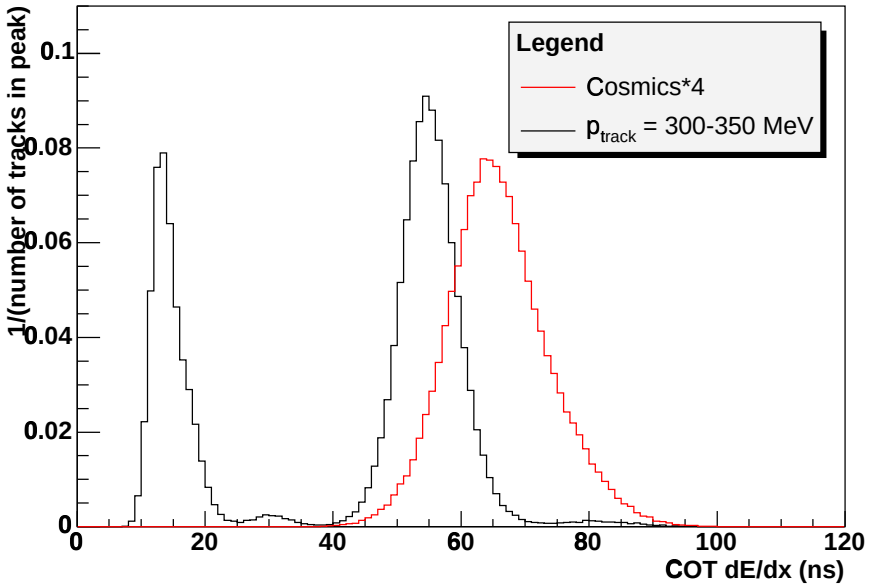

Figure 5.3: Comparison of dE/dx values for highly ionizing proton sample and highly ionizing muon sample (Cosmic $\times$ 4). Since the peaks are not aligned, any efficiency calculated from the proton sample is to be taken as an underestimate of the true $COTHW$ efficiency for doubly-charged Higgs events.

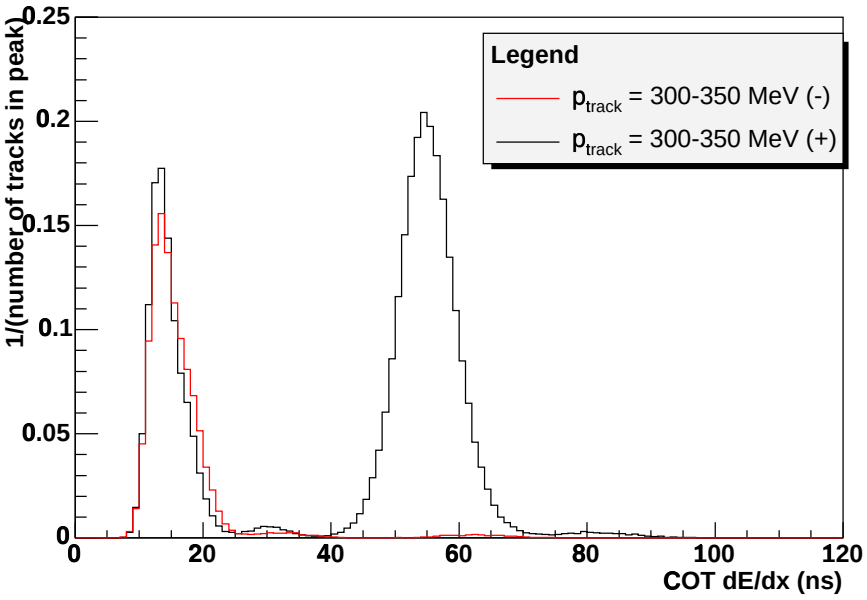

Figure 5.4: Comparison of positively and negatively charged particles in the momentum window of 300-350 MeV. We will use the proton-antiproton assymetry to remove the pion and kaon contamination.

the interaction point, we compute a single tower surface area of about 1,000 cm^2. Considering only the area of this tower within 0.5 cm of the edge, we get 70 cm^2, which is only 7% of the total area. A doubly-charged Higgs as seen by the detector would have a mean p_T of about 50 GeV and would deposit, on average, roughly 9 GeV in the calorimeters (four times the average of a cosmic). As a result, the $H^{\pm\pm}$ would fail the isolation ratio cut roughly 5 percent of the time. To account for this potential effect causing the doubly-charged Higgs to fail the isolation cut roughly 75% of the time it passes through an edge, we change the track efficiency from its current value of $93.6 \pm 0.2\%$ to $89 \pm 5\%$. As for multiple scattering, which could potentially affect the $|dx|$ cuts on the stub, for upsilon tracks having $p_T < 20$ GeV no reduction in efficiency was observed. In this study, a change in p_T by a factor of three makes no significant difference. The $H^{\pm\pm}$ p_T is larger than these upsilons,

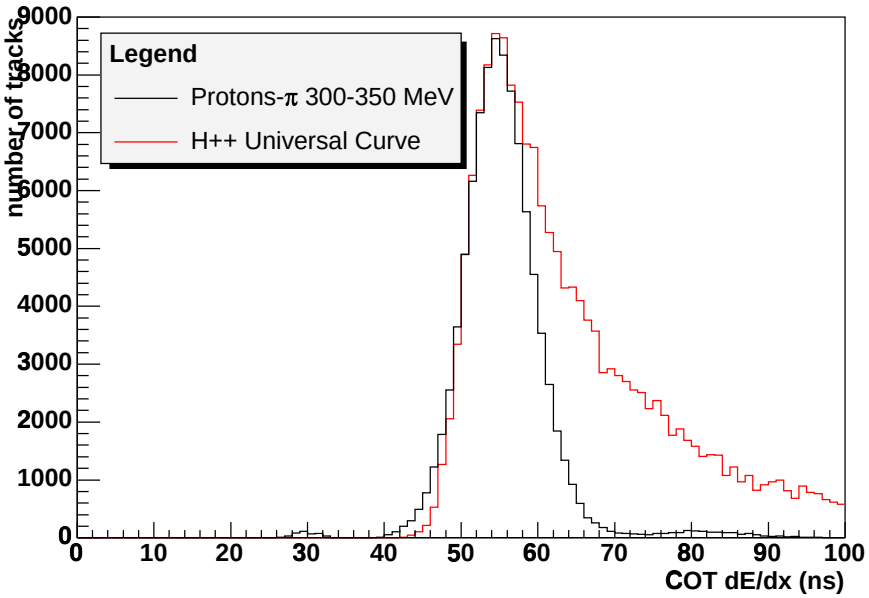

Figure 5.5: The subtracted proton distribution (positively charged particles - negatively charged particles) used for measuring $H^{\pm\pm}$ efficiency. Some residual kaons produce the bump to the left of the primary peak. The peak of the distribution matches nicely with the $H^{\pm\pm}$ Universal Curve theoretical prediction.

thus we expect negligible inefficiency due to multiple scattering.

Since both particles come from the same vertex, the $|z_0|$ efficiency can stand as it is, but the Track Cuts are required of each particle separately, so we must square this efficiency to find the net Z efficiency. The same applies for all of the high ionization cuts, since each particle must pass the cut. These efficiencies are summarized in Table 5.4. The Trigger and Stub Cuts are only required for at least one of the two particles, therefore we need to calculate these efficiencies using the binomial formula:

$$\begin{aligned} \mathrm{P(at\ least\ one)} &= 1 - \mathrm{P(neither)} \\ &= 1 - \big(1-\epsilon_1\big)\big(1-\epsilon_2\big) \end{aligned} \tag{5.2}$$

where ϵ_1 and ϵ_2 are the Trigger and Stub efficiencies corresponding to the muon detectors being considered. For example, if both of the particles pass through the CMUP, then the efficiency for at least one of them triggering and leaving a stub would be found by using the CMUP Trigger and Stub efficiency for both ϵ_1 and ϵ_2 in Equation 5.2. The three possible categories (CMUP×2, CMX×2, and CMUP/CMX) for this efficiency have been calculated and can be found in Table 5.5, along with the fraction of $H^{\pm\pm}$ MC measured for each category.

Selection Criteria	Loose Efficiency (%)	Tight Efficiency (%)
$\lvert z_0\rvert < 60$ cm	95.0 ± 0.4	95.0 ± 0.4
All Track Cuts	79.2 ± 10.0	79.2 ± 10.0
EMET & HadET Cuts	-	65.76 ± 0.09
COTHW cut	$100.0^{+0.0}_{-1.0}$	$100.0^{+0.0}_{-1.0}$
All above	75.2 ± 9.5	49.5 ± 6.3

Table 5.4: $H^{\pm\pm}$ ID efficiencies except for CMUP/CMX Trigger and Stub efficiencies which are dependent on the Higgs mass and can be found in Table 5.5.

$H^{\pm\pm}$ mass	ϵ_{CMUP}	CMUP×2 fraction	ϵ_{CMX}	CMX×2 fraction
90 GeV	0.955 ± 0.003	0.582 ± 0.005	0.997 ± 0.001	0.066 ± 0.002
100 GeV	0.955 ± 0.003	0.574 ± 0.005	0.997 ± 0.001	0.070 ± 0.002
130 GeV	0.955 ± 0.003	0.593 ± 0.004	0.997 ± 0.001	0.064 ± 0.002
160 GeV	0.955 ± 0.003	0.603 ± 0.004	0.997 ± 0.001	0.063 ± 0.002

$H^{\pm\pm}$ mass	$\epsilon_{CMUP/CMX}$	CMUP/CMX fraction	Net Trigger Eff.
90 GeV	0.987 ± 0.002	0.352 ± 0.004	0.969 ± 0.007
100 GeV	0.987 ± 0.002	0.355 ± 0.004	0.968 ± 0.007
130 GeV	0.987 ± 0.002	0.342 ± 0.004	0.968 ± 0.006
160 GeV	0.987 ± 0.002	0.334 ± 0.004	0.968 ± 0.006

Table 5.5: CMUP and CMX Trigger and Stub efficiencies with their fraction of occurence in the $H^{\pm\pm}$ Monte-Carlo having masses of 90, 100, 130, and 160 GeV. ϵ_{CMUP} is the efficiency for both particles in the CMUP detector, ϵ_{CMX} for both particles in the CMX detector, and $\epsilon_{CMUP/CMX}$ is the efficiency for one particle in each detector.

$H^{\pm\pm}$ mass	Net Loose $H^{\pm\pm}$ Efficiency	Net Tight $H^{\pm\pm}$ Efficiency
90 GeV	0.729 ± 0.092	0.480 ± 0.061
100 GeV	0.728 ± 0.092	0.479 ± 0.061
130 GeV	0.728 ± 0.092	0.479 ± 0.061
160 GeV	0.728 ± 0.092	0.479 ± 0.061

Table 5.6: Net $H^{\pm\pm}$ ID efficiencies using either loose or tight ionization cuts. These were calculated from the efficiencies listed in Tables 5.4 and 5.5.

5.2 Acceptance

Acceptance describes the ability of a detector to detect and measure the properties of all particles that are generated in a collision. Particles can be lost in certain empty regions between detectors or even in the cracks between detector segments

where readout wires run. It would be impossible to measure acceptance using real particles in the detector, since there is no mechanism for knowing how many particles the detector did not see. Instead, a Monte-Carlo technique is used whereby a very large number of simulated particles are measured by a simulated detector and then sent through offline processing as if they were the real data. Finding the acceptance using this technique merely involves calculating the ratio of reconstructed to generated particles. The procedure is described in fuller detail and with supporting data below.

5.2.1 $H^{\pm\pm}$ Monte-Carlo Acceptance

We use 50,000 Monte-Carlo events generated with PYTHIA to determine the CDF Run II detector acceptance for finding doubly-charged Higgs particles. In order to properly simulate a quasi-stable, doubly-charged Higgs, something needs to be done to the particle when creating it in PYTHIA to prevent immediate decay. We generate H^{++}/H^{--} pairs having masses of 100 GeV, then immediately change their particle ID, mass, and energy to cause them to look like muons when passing through CDFSIM. In this way, we preserve the doubly-charged Higgs kinematics while allowing for stable particles. We also halve the momentum of each generated particle to account for it's doubled charge.

The kinematics of a $Z^0 \rightarrow H^{++}H^{--}$ event are quite different from that of a $Z^0 \rightarrow \mu\mu$ event. The large mass of the generated particles allows for a high generated p_T distribution, as can be seen in Figures 5.6 and 5.7. Figure 5.6 shows the apparent p_T distribution that the detector sees, and Figure 5.7 shows the true p_T of the doubly-charged Higgs.

Also, the doubly-charged Higgs have a much narrower η spectrum compared

to their muon counterparts in Figure 5.9. These two kinematic differences are instrumental in increasing the acceptance of the $Z^0 \rightarrow H^{++}H^{--}$ events. Since we use $Z^0 \rightarrow \mu\mu$ events in the calculation of our tracking efficiency, we show the η dependence of this efficiency in Figure 5.10. Since this figure is quite flat over the region of interest, we do not modify our efficiency based on the more narrow η distribution of the $H^{\pm\pm}$.

The Higgs are slower than muons as can be seen in the $\beta\gamma$ distributions at 100 and 160 GeV masses in Figure 5.8. Track reconstruction efficiency falls off gradually beginning with $\beta\gamma < 0.4$ due to failures in pattern recognition [16]. Fewer than 3.5% of our 160 GeV $H^{\pm\pm}$ (and fewer than 2% of 100 GeV ones) are slow enough to be in this lower-efficiency region, making the acceptance loss of slow Higgs only a fraction of a percent. This small effect is completely dominated by other systematic errors in the analysis.

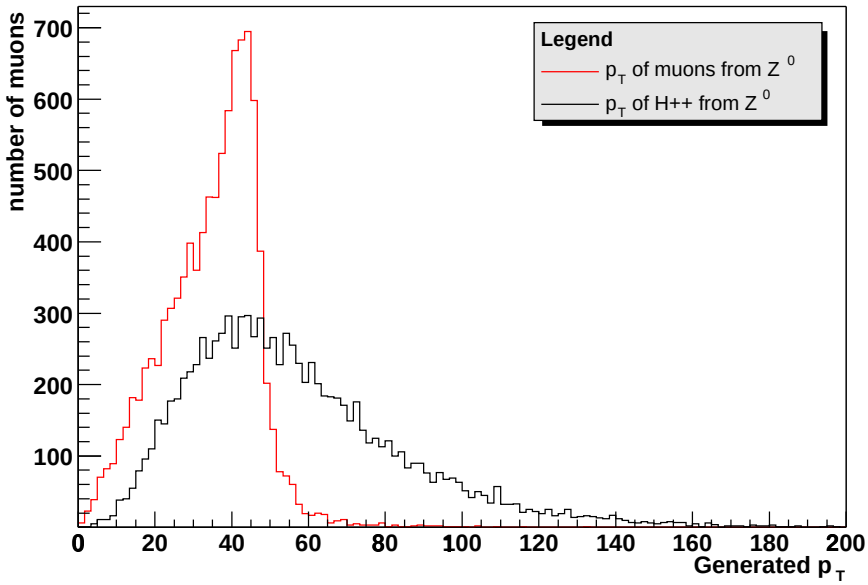

Figure 5.6: The generator level p_T for muons from Z^0 and the apparent generator level p_T for 100 GeV doubly-charged Higgs from Z^0 as seen by the detector.

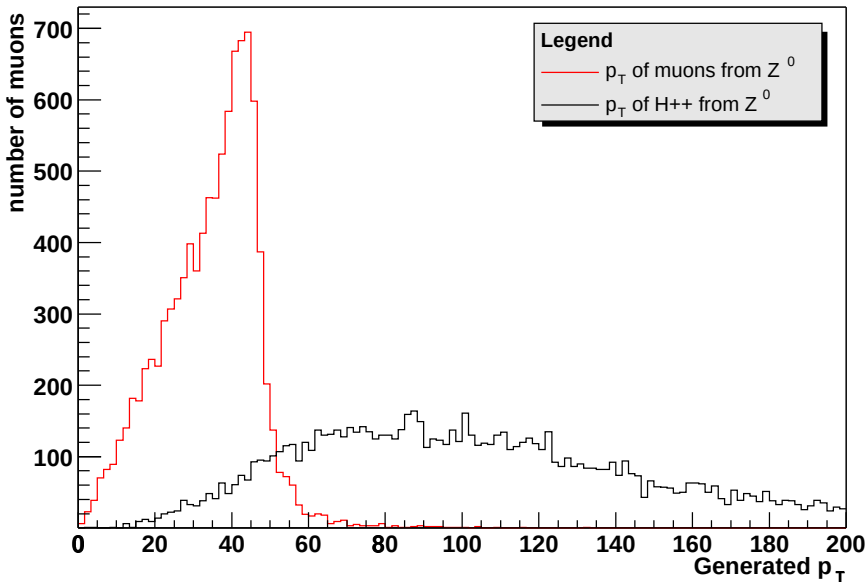

Figure 5.7: The generator level p_T for muons from Z^0 and the true generator level p_T for 100 GeV doubly-charged Higgs from Z^0.

5.2.2 Measuring Doubly-Charged Higgs Acceptance

The kinematic and geometric cuts which we used in selecting our sample were as follows:

- z position of vertex $|z_0| < 60$ cm
- Reconstructed "muon" track with CMUP or CMX stub
  - COT exit radius $\rho_{COT} > 140$ cm
  - CMP/CMX fiducial "muon"
  - "Muon" track $p_T > 20$ GeV/c
- Second reconstructed "muon" track

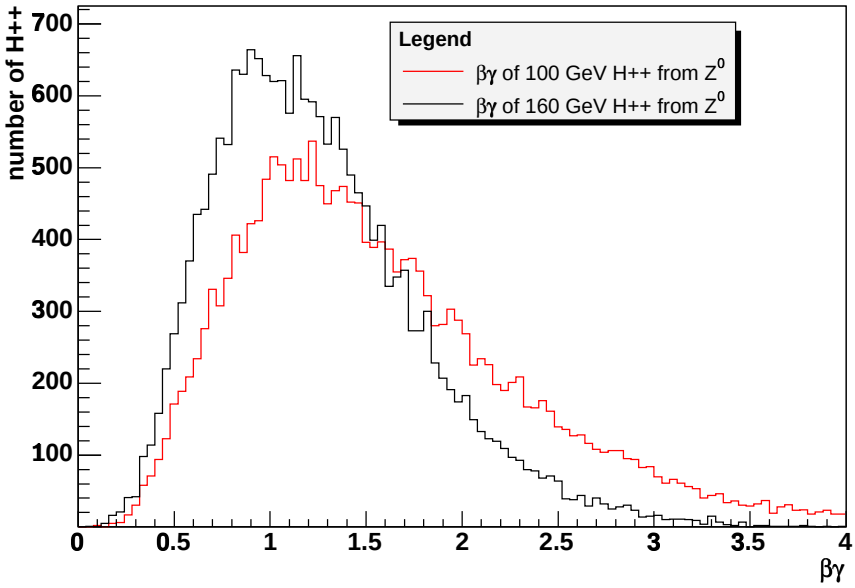

Figure 5.8: The $\beta\gamma$ distributions from Monte Carlo of $Z^0 \rightarrow H^{++}H^{--}$ having masses of 100 and 160 GeV.

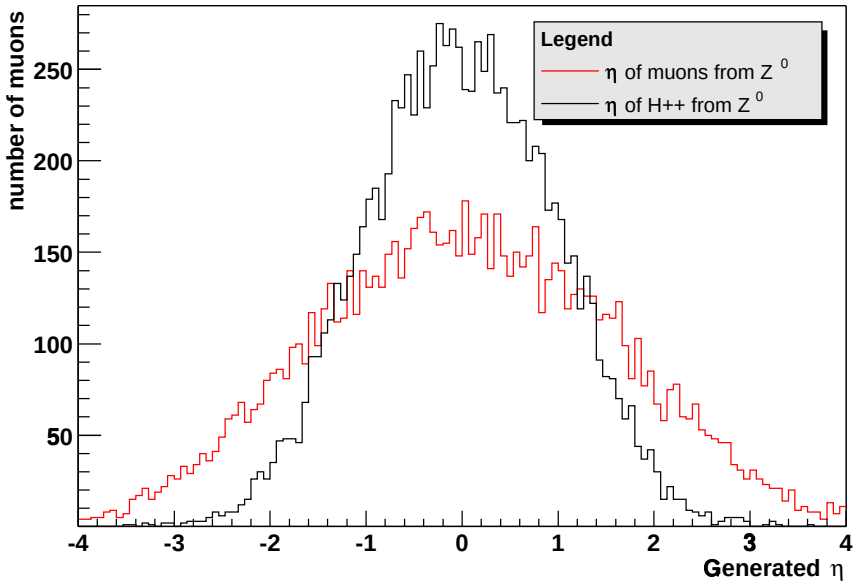

Figure 5.9: The generated η distributions from Monte Carlo of $Z^0 \rightarrow H^{++}H^{--}$ and $Z^0 \rightarrow \mu\mu$.

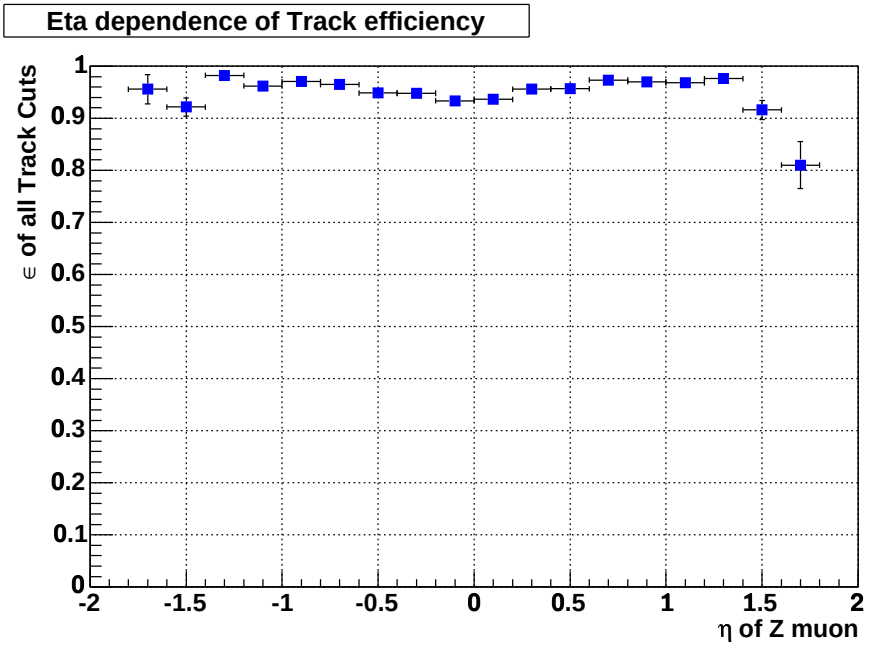

Figure 5.10: The tracking efficiency as a function of η for $Z^0 \rightarrow \mu\mu$ data.

- COT exit radius $\rho_{COT} > 140$ cm
- "Muon" track $p_T > 20$ GeV/c

These acceptance cuts are identical to the cuts used in calculating acceptance for Z's by the cross-section group in [17]. The ID cuts in Section 4.3 are not made when calculating the acceptance. It is to be interpreted as a pure geometric and kinematic acceptance. Table 5.7 and Figure 5.11 show the product of acceptance and efficiency for both the loose and tight topologies. The efficiencies listed are weighted by the distribution of events in the MC.

From these calculated acceptances, we can predict the number of $H^{\pm\pm}$ events we expect to see in the data. Table 5.8 shows these predictions at our four mass points.

$H^{\pm\pm}$ mass	Acceptance	Net Loose Efficiency	Loose Acc×Eff
90 GeV	0.3843 ± 0.0023	0.729 ± 0.092	0.280 ± 0.035
100 GeV	0.3951 ± 0.0023	0.728 ± 0.092	0.288 ± 0.036
130 GeV	0.4335 ± 0.0023	0.728 ± 0.092	0.316 ± 0.040
160 GeV	0.4681 ± 0.0023	0.728 ± 0.092	0.341 ± 0.043

$H^{\pm\pm}$ mass	Acceptance	Net Tight Efficiency	Tight Acc×Eff
90 GeV	0.3843 ± 0.0023	0.480 ± 0.061	0.184 ± 0.023
100 GeV	0.3951 ± 0.0023	0.479 ± 0.061	0.189 ± 0.024
130 GeV	0.4335 ± 0.0023	0.479 ± 0.061	0.208 ± 0.026
160 GeV	0.4681 ± 0.0023	0.479 ± 0.061	0.224 ± 0.029

Table 5.7: Acceptances, net efficiencies, and their product for long-lived doubly-charged Higgs corresponding to either loose or tight search cuts having masses of 90, 100, 130, and 160 GeV respectively.

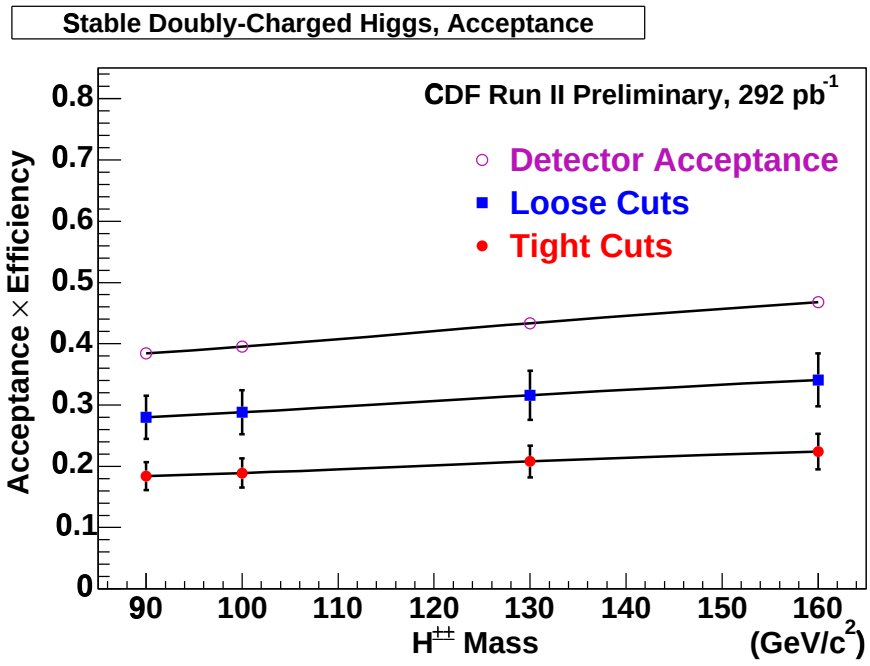

Figure 5.11: Plot of the product of acceptance and efficiency corresponding to loose and tight ionization cuts. Also shown is the net fiducial and kinematic acceptance at various $H^{\pm\pm}$ masses before efficiencies are included.

$H^{\pm\pm}$ mass	Loose $H^{\pm\pm}$ Events Expected	Tight $H^{\pm\pm}$ Events Expected
90 GeV	21.6 ± 3.5	14.2 ± 2.3
100 GeV	14.7 ± 2.4	9.6 ± 1.6
130 GeV	5.3 ± 0.8	3.5 ± 0.6
160 GeV	2.2 ± 0.4	1.4 ± 0.2

Table 5.8: Number of stable doubly-charged Higgs expected in the data, corresponding to either loose or tight search cuts having masses of 90, 100, 130, and 160 GeV.

5.3 Systematics

There are several sources of systematic uncertainties in the analysis. Here we measured the relative errors introduced by these uncertainties. We considered these sources: luminosity, K factor, PDF cross section, PDF acceptance, trigger efficiency, Z_{vtx} efficiency, ID efficiency, cosmic efficiency, energy scale, and energy resolution. Since all these sources of error contribute to the uncertainty applied to our Bayesian analysis, we list them here in one place. We find it necessary to point out though that both the K factor and PDF cross section errors correspond only to the theory cross-section and are not included with the others in the net systematic error on the experimental cross section.

5.3.1 Luminosity

The luminosity of our data sample with the run declared good for both the CMUP and CMX detectors was measured to be $292.0 \pm 16.6\ pb^{-1}$ [15]. The total uncertainty on this integrated luminosity is 6%, where 4.4% is from the acceptance and 4% is from the inelastic cross section [18].

5.3.2 K Factor

The theoretical cross sections at next-to-leading-order (NLO) for the doubly charged Higgs contain systematic errors coming from renormalization and factorization scale dependence which were estimated at the time of their calculation to be between $5-10\%$ [20]. For our systematic error, we took the central value in the stated range, 7.5%.

5.3.3 PDF Cross Section

The uncertainty on the cross section results from the parton distribution function (PDF). We chose to use CTEQ6L as the PDF for our central value. We investigated the effect of different PDF choices by folding in the cross section errors from the 40 alternate eigenvectors in CTEQ6 following the EWK prescription [19]. We generated 100,000 events for each of the 41 PDF's at each of our mass points. The systematic errors for each mass point are shown in Table 5.9.

5.3.4 PDF Acceptance

The acceptance also depends on chosen PDF. To calculate this error, we found the generator level acceptance of the 100,000 events generated above for each mass point and eigenvector. We again followed the EWK prescription for calculating the acceptance uncertainty due to PDF's and list the errors we find in Table 5.9.

5.3.5 Trigger & Stub Efficiency

The trigger and stub efficiencies for the triggers used in our analysis (MUON_CMUP_18 and MUON_CMX_18) were weighted by the fiducial distribution of $H^{\pm\pm}$ MC in Ta-

ble 5.5. Our net trigger efficiencies for $H^{\pm\pm}$ having masses of 90, 100, 130, and 160 GeV were 0.965 ± 0.007, 0.964 ± 0.007, 0.963 ± 0.006, and 0.964 ± 0.006 respectively. These translate to systematic errors on the acceptance of 0.73%, 0.73%, 0.62%, and 0.62% at the four mass values.

5.3.6 Z_{vtx} Efficiency

The Z vertex efficiency has been measured to be $.950 \pm 0.004$ [17]. From this measurement we calculate the relative systematic error on the net acceptance to be 0.42% for all mass points considered.

5.3.7 Identification Efficiency

The ID efficiency (excluding the Z vertex efficiency shown above) was calculated to be $.504 \pm .062$ from its three remaining components in Table 5.4. Each of the three efficiencies comprising this ID efficiency were found by squaring the efficiency for a single particle to pass the cut. The statistical error on this efficiency results in a systematic error on the acceptance of 12.3%.

5.3.8 Cosmic Efficiency

The upper bound on the inefficiency of the cosmic tagger used has been measured to be 0.8% [15]. This bound can be used to estimate a systematic uncertainty for the cosmic-rejection algorithm on the acceptance of doubly-charged Higgs events.

5.3.9 Energy Scale

To find the systematic error due to energy scale uncertainty, we began by finding the di-muon mass distribution for $Z \rightarrow \mu\mu$ candidates in the data compared to simulated $Z \rightarrow \mu\mu$ events. Fitting a gaussian to this distribution between 82 and 100 GeV, we found the mean value for the Z mass peak to be 90.782 ± 0.054 GeV for data candidates and 90.887 ± 0.021 GeV for MC events. Thus, we applied a scale factor of 0.9988 to the simulated energies which resulted in a scaled Z mass peak of 90.782 ± 0.021 GeV for MC events. We measured the change in the energy scale factor that would be needed to shift the Z mass peak in the simulation by twice the statistical error on the mean mass in the data ($0.054 \times 2 = 0.108$). Scaling the energies by $\pm 0.125\%$ was found to accomplish this, so we included this additional scale factor in the MC energies to determine the effect of the energy scale errors on the acceptance. We recalculated our acceptances with this additional shift of $\pm 0.125\%$ on the energies. Since this energy scale spread corresponds to a shift of four standard deviations, we divided the net change in acceptance by 4 to find the error this uncertainty contributes. The contributed systematic error at each mass can be seen in Table 5.9.

5.3.10 Energy Resolution

The systematic error due to energy resolution uncertainty was derived in much the same way as energy scale above. Now, instead of scaling the mean of the Z peak so the simulation matches the data, we applied a gaussian smear so the RMS widths remain the same. A gaussian fitted to the Z mass peak between 82 and 100 GeV had an RMS width of 3.81 ± 0.05 GeV in the data and 3.28 ± 0.02 GeV in the simulation. We found that smearing the energies in the simulation by 1.90% increased its RMS

width to 3.80 ± 0.02, thus matching the data width to well within the statistical errors. We also found the change required in the energy smearing to increase or decrease the MC width by twice the statistical error on the data ($0.05 \times 2 = 0.10$). Smearing the energies by $\pm 0.35\%$ increased and decreased the simulation width by these 2 standard deviations, so we applied this additional smearing factor to the $H^{\pm\pm}$ MC to determine its effect on the acceptances. We divided the net change in acceptance for each mass point by 4, since four standard deviations separate the two values and include the resulting uncertainty on the acceptance in Table 5.9.

5.3.11 Systematic Summary

Table 5.9 summarizes all uncertainty contributions resulting from each source of error at our three mass values. We added the individual errors in quadrature to determine the total systematic error for each mass point. The net systematic errors include errors to both the experimental and theoretical cross sections. While we realize that the theoretical errors are not a part of the experimental cross sections, we combined them as such so the Bayesian analysis to follow can incorporate as many of the errors as possible in its single error input. Table 7.1 shows the separation of these errors to the respective cross sections, both experimental and theoretical.

Systematic	90 GeV $H^{\pm\pm}$	100 GeV $H^{\pm\pm}$	130 GeV $H^{\pm\pm}$	160 GeV $H^{\pm\pm}$
Luminosity	6	6	6	6
K factor	7.5	7.5	7.5	7.5
σ_{PDF}	4.49	4.80	5.06	5.55
PDF acc.	1.15	1.13	0.98	0.95
Trigger eff.	0.73	0.73	0.62	0.62
Z_{vtx} eff.	0.42	0.42	0.42	0.42
ID eff.	12.3	12.3	12.3	12.3
Cosmic eff.	0.8	0.8	0.8	0.8
E scale	0.006	0.0005	0.0005	0.0005
E resolution	0.005	0.004	0.0006	0.001
Total	16.6	16.7	16.8	16.9

Table 5.9: Summary of all systematic uncertainties. Errors shown are relative errors in percentages. Total errors for each mass point were found by adding the individual errors in quadrature for the corresponding mass, except for σ_{PDF} and PDF acceptance which are expected to be correlated so were added linearly. These totals are the cumulative theoretical and experimental errors used in our Bayesian analysis.

Chapter 6

Backgrounds to $H^{\pm\pm}$ Signal

The pollution of the search region by other non-signal particles is referred to as background. It is a natural byproduct of the desire to increase the efficiency of the search by using a finite number of selection cuts. We desire that only the "best" events, those with a high signal to background ratio, are able to pass these cuts for inclusion in the final analysis. Thus, a delicate balance must be struck between efficiency and background levels in order for the search to be as effective as possible. To determine the total background for the search, the individual backgrounds for each potential source must be separately calculated and summed.

6.1 Fake Rates

In order to determine the $H^{\pm\pm}$ backgrounds, we calculated individual fake rates for all long-lived particles that could also be measured in the detector as highly ionizing. A fake rate is defined as the ratio of the potential background count that pass all $H^{\pm\pm}$ selection cuts, divided by the total number of particles to which the cuts are applied. Once the fake rate is determined, we can then derive the expected number of background particles by finding the product of the number of fakable events and the fake rate. In this section we describe the measurement of four different fake

rates for each of the four expected classes of background in the search: muons, electrons, taus, and QCD jets.

6.1.1 Measuring Muon $\rightarrow H^{\pm\pm}$ Fake Rates

We selected cosmic rays from CDF Run II data (sample defined in Section 4.1.2) as a pure muon sample for this fake rate measurement. The cosmics were tagged using tightened selection cuts from the COT cosmic-ray tagger [14]. We selected cuts on our three dE/dx variables to identify high ionization tracks. The respective fake rates for the cuts are then measured by observing how many cosmics in the sample pass these high ionization cuts.

We also include a representation of a high ionization sample in our figures by multiplying the dE/dx quantity for each cosmic by a factor of four and plotting that histogram together with the original cosmic histogram. This gives a description of how the signal for a doubly-charged particle should look. Figure 6.1 gives these histograms for $EMET$ along with the cut value chosen, while Figures 6.2 and 6.3 show the same for $HadET$ and $COTHW$ respectively. The high ionization cuts are listed in Table 4.4. The $H^{\pm\pm}$ selection includes the track and stub cuts in Table 4.2 and these high ionization cuts in Table 4.4.

Fake rates were calculated by counting the number of cosmic events passing (above) the respective cut values. Fake rates were also found for combined variables, and these rates confirm that our three variables are not highly correlated. All the relevant fake rates are shown in Table 6.1.

Efficiencies were also calculated for these high ionization cuts and are given in Section 5.1.

In order to find an upper limit for the fake rate on the combined ionization cuts,

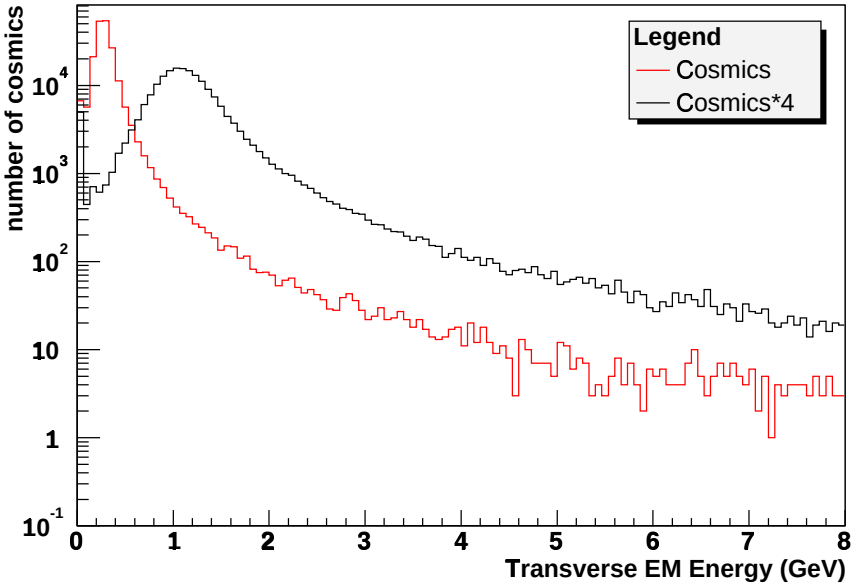

Figure 6.1: Out of 216,224 cosmic events, 11,612 passed the 0.6 GeV cut on $EMET$. This gives a fake rate for this variable alone of $(5.37 \pm 0.05)\%$. Of the "Cosmics $\times$ 4" events 184,321 passed the same cut, giving a signal efficiency of $(85.25 \pm 0.08)\%$.

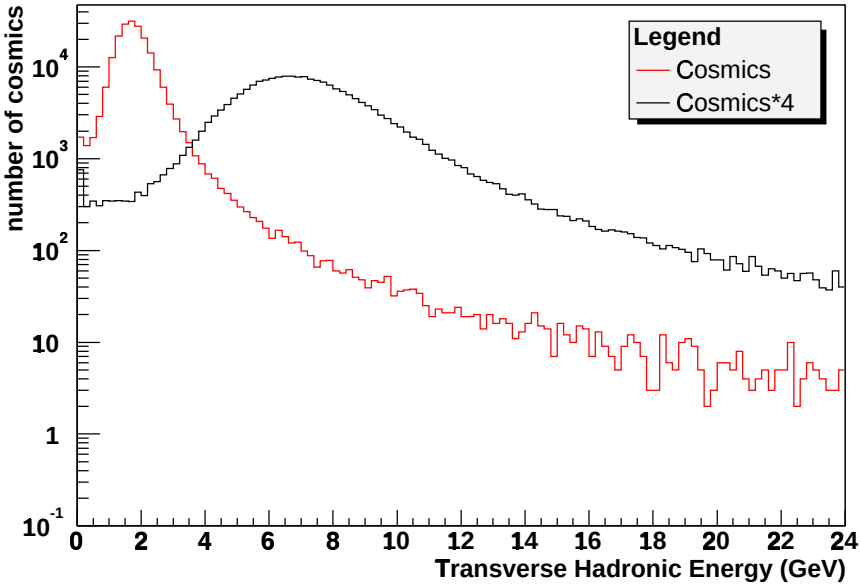

Figure 6.2: Out of the same 216,224 cosmics, only 6,486 passed the 4 GeV cut on *HadET*. Thus, the fake rate for this variable was found to be $(3.00 \pm 0.04)\%$. Of the highly ionizing "Cosmics $\times$ 4" events, 191,790 passed the cut, giving a signal efficiency of $(88.70 \pm 0.07)\%$.

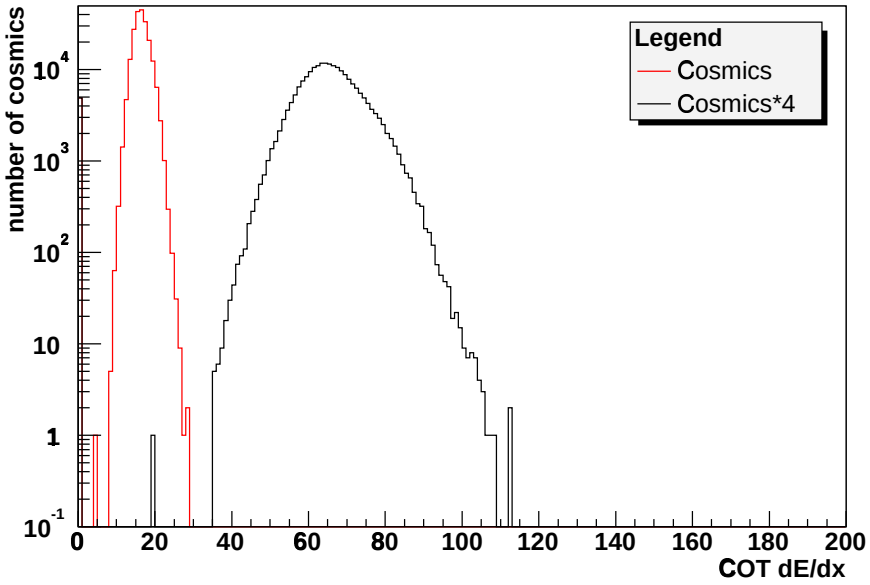

Figure 6.3: None of the 216,224 cosmics passed the 35 ns $COTHW$ cut, therefore the individual fake rate for this variable is 0%. The experimental limits of recording very small pulse widths do not permit us to use this sample for measuring $COTHW$ cut efficiency.

we lowered the cut value of $COTHW$ to 20 ns. Using this cut value, we found the combined fake rate of all three variables to be $(0.01619 \pm 0.00274)\%$ which is estimated to be high by a factor of roughly 10,000 (since there were 10,566 fakes for the $COTHW$ variable alone when cut at 20 ns and on the order of 1 fake when cut at 35 ns). Thus, the fake rate of the combined variables with all high ionization cuts listed in Table 4.4 is estimated to be:

$$\begin{aligned} \text{Net } \mu \rightarrow H^{\pm\pm} \text{ fake rate} &= f_1 \times f_2 \\ &= (1.5 \pm 1.5) \times 10^{-8}, \end{aligned} \tag{6.1}$$

where f_1 is the fake rate given in the sixth line of Table 6.1 and f_2 is from the eighth line of the same table. f_2 is not calculated from the entire cosmics sample, but only from those events passing the 20 ns $COTHW$ cut. Their product is the bottom line of that table and is the same as that in Equation 6.1 above. Thus it is apparent that the fake rate due to highly ionizing muons is quite small.

Variable(s) cut	Cut value	# Passing	Tight μ Fake rate (%)
Cosmic Tagger		216,224	
EMET	> 0.6 GeV	11,612	5.37 ± 0.05
HadET	> 4 GeV	6,486	3.00 ± 0.04
EMET & HadET	above	763	0.353 ± 0.013
COTHW	> 20 ns	10,566	4.89 ± 0.05
EMET, HadET, & COTHW	above	35	0.01619 ± 0.00274
COTHW	> 20 ns	10,566	
COTHW	> 35 ns	0 (1 ± 1)	0.00946 ± 0.00946
Tight Ionization	Table 4.4	0	$(1.5 \pm 1.5) \times 10^{-6}$

Table 6.1: Muon $\rightarrow H^{\pm\pm}$ fake rates with tight ionization cuts.

Variable(s) cut	Cut value	# Passing	Loose μ Fake rate (%)
Cosmic Tagger		216,224	
COTHW	> 35 ns	$0\ (1 \pm 1)$	$(4.6 \pm 4.6) \times 10^{-4}$
Loose Ionization	Table 4.4	0	$(4.6 \pm 4.6) \times 10^{-4}$

Table 6.2: Muon $\rightarrow H^{\pm\pm}$ fake rates with loose ionization cuts.

6.1.2 Muon $\rightarrow H^{\pm\pm}$ Fake Rate Systematics

To further understand high ionization for muons passing through the COT, we did a systematics study of the $COTHW$ variable. For this study we lowered the $COTHW$ cut to 20 ns in order to introduce some cosmics having higher ionization so a fake rate could be calculated. Then we plotted this modified fake rate as a function of three variables.

The first relationship we analyzed was that between fake rate and COT track multiplicity. This quantity is defined as the number of tracks with at least one hit in the COT. Figure 6.4 illustrates the rise in the fake rate as a direct result of more tracks in the COT. This is possibly due to the merging of nearby hits thus artificially increasing the pulse-width. Figure 6.5 shows that the Z and W events are much more track-rich than the cosmic events which we used to calculate the fake rate, therefore we need to scale our fake rate to a higher value. To do this, we found the mean of the track multiplicity for both the W and Z event candidates to be roughly 30 tracks. The appropriate $COTHW$ fake rate to use for this increased number of tracks in the COT was taken from Figure 6.4 to be $7.00 \pm 0.07\%$. The error on this rate was found by scaling the error on the fake rate for $COTHW$ (20 ns cut) found using cosmic events (0.05%) by the ratio of the new fake rate (7.00%) to the old (4.89%). The net fake rate using all the high ionization cuts in

Table 4.4 also must be scaled by this ratio, giving us new $\mu \rightarrow H^{\pm\pm}$ fake rates of $(2.1 \pm 2.1)\% \times 10^{-6}$ for the tight search and $(6.6 \pm 6.6)\% \times 10^{-4}$ for the loose.

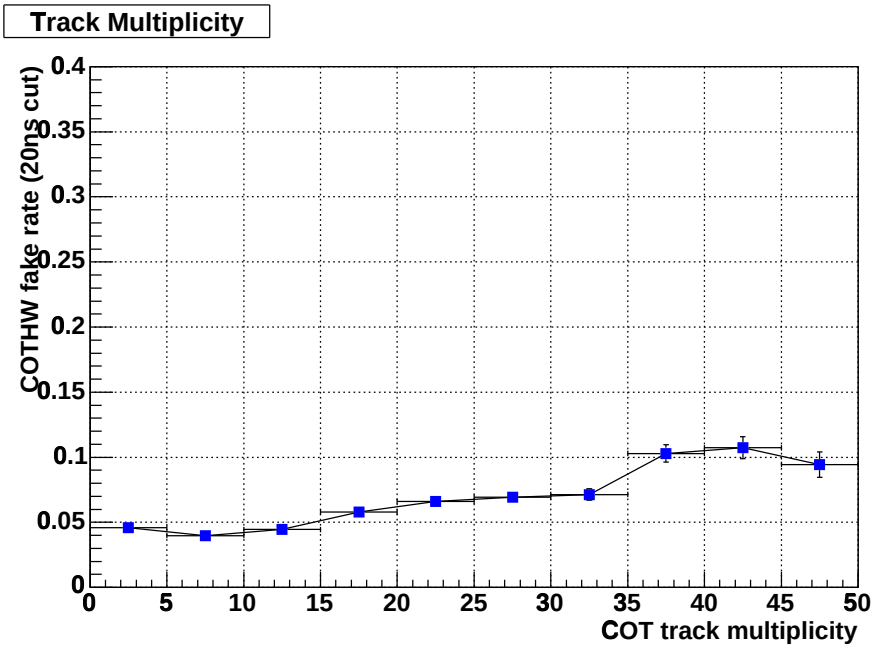

Figure 6.4: Systematic of $COTHW$ showing the clear increase in fake rate as more tracks populate the COT.

We also examined COT track density in the 0.4 cone surrounding the muon. These tracks are more likely to directly effect the ionization in the COT by artificially widening the muon's pulse width. Only tracks having at least one COT hit are counted, and we include the primary track in this value. We show the corresponding fake rate distribution for cosmics by the number of tracks found in the cone in Figure 6.6. The number of tracks in this cone for Z, W, and cosmic events can be seen in Figure 6.7. Again, the fake rates increase as the number of tracks in the cone increases, prompting us to scale our cosmic sample fake rate up for collider events. We find the mean number of tracks in the cone for W and Z events to be 1.85 tracks (with only 1.14 tracks on average in cosmic events). We take the $COTHW$ fake rate for 2 tracks in the cone (from Figure 6.6) of $5.92 \pm 0.19\%$. Scaling up our final $\mu \rightarrow$

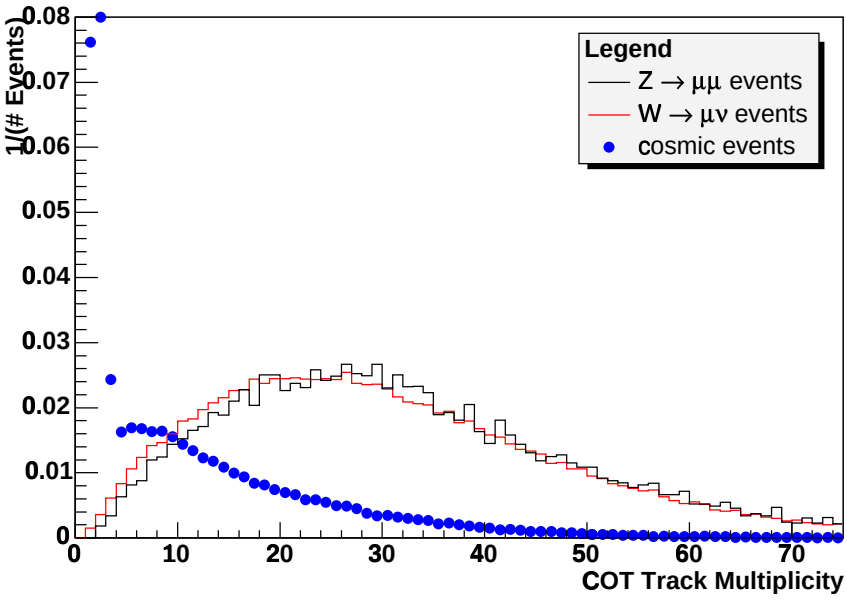

Figure 6.5: Comparison of relative COT track multiplicities for Z events, W events, and cosmic events. The mean track multiplicities for Z and W events were found to be 30.8 and 29.6 respectively.

$H^{\pm\pm}$ fake rate by the ratio between this new fake rate and the old $COTHW$ fake rate of $4.89\pm0.05\%$ results in a scaled fake rate of $(1.8\pm1.8(stat)\pm0.3(syst))\%\times10^{-6}$ for the tight search and $(5.6 \pm 5.6(stat) \pm 1.0(syst))\% \times 10^{-4}$ for the loose. We use these fake rates in place of the ones scaled by track multiplicity above, and give systematic errors based on the difference between the two methods of scaling for track density.

Similarly, isolation fraction measures how much energy is deposited in a window surrounding the track in question and is also a good quantity for this systematics study. Figure 6.8 shows the fake rate measured by $COTHW$ as a function of the isolation fraction. It appears from this figure that the fake rate is not highly correlated to this variable.

The final systematic comparison studies the fake rate as a function of the total

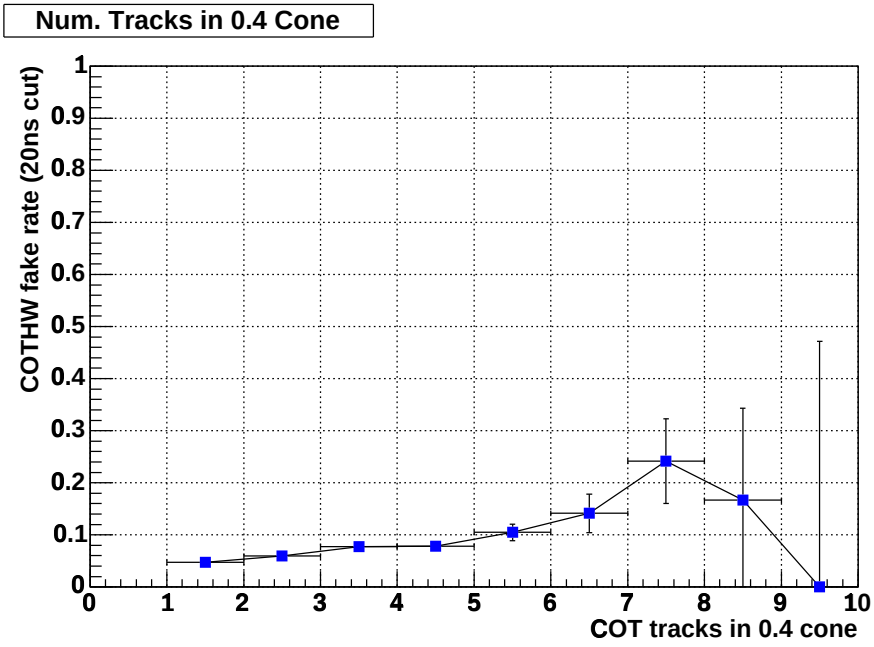

Figure 6.6: Systematic of $COTHW$ showing the clear increase in fake rate as more tracks surround the muon track.

energy deposited by the muon in the hadronic and electromagnetic calorimeters. Since this is a calorimetric quantity, we expect it to be relatively flat if the $COTHW$ fake rate is not highly correlated to the calorimetric dE/dx quantities and Figure 6.9 confirms this.

6.1.3 Measuring Electron $\rightarrow H^{\pm\pm}$ Fake Rates

We use $W \rightarrow e\nu$ Monte-Carlo events ($\sim$ 1,150,000 events from the `wtop0e` dataset) as an electron sample for this fake rate measurement. We look in this electron sample for reconstructed "muons" passing the Track Cuts from Table 4.2. Upon making the Track Cuts we calculated the fake rate by counting the fraction which also pass the Stub Cuts in Table 4.2 and the three high ionization cuts in Table 4.4.

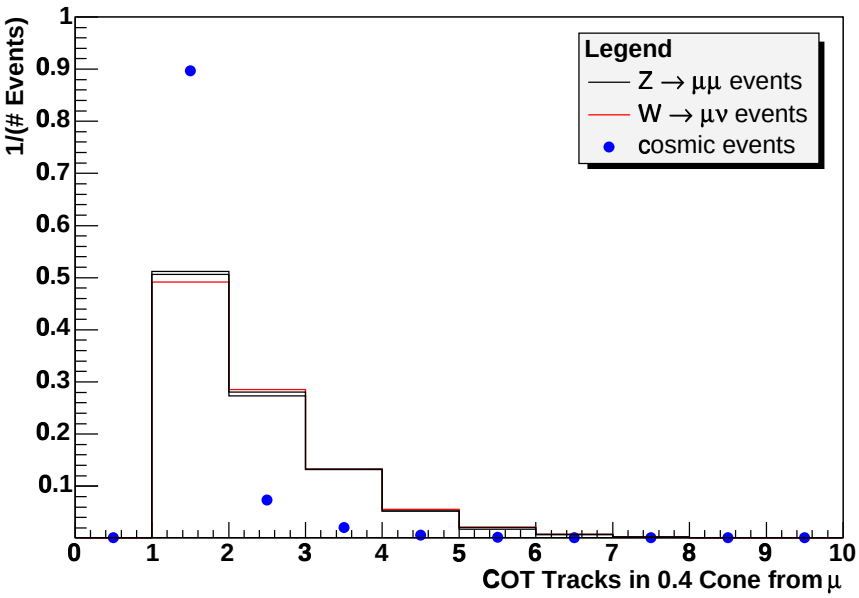

Figure 6.7: Comparison of relative number of COT tracks in 0.4 cone for Z events, W events, and cosmic events. The mean number of tracks in the cone for Z and W events were found to be 1.83 and 1.88 respectively, with only 1.14 tracks in the cone on average for cosmic events.

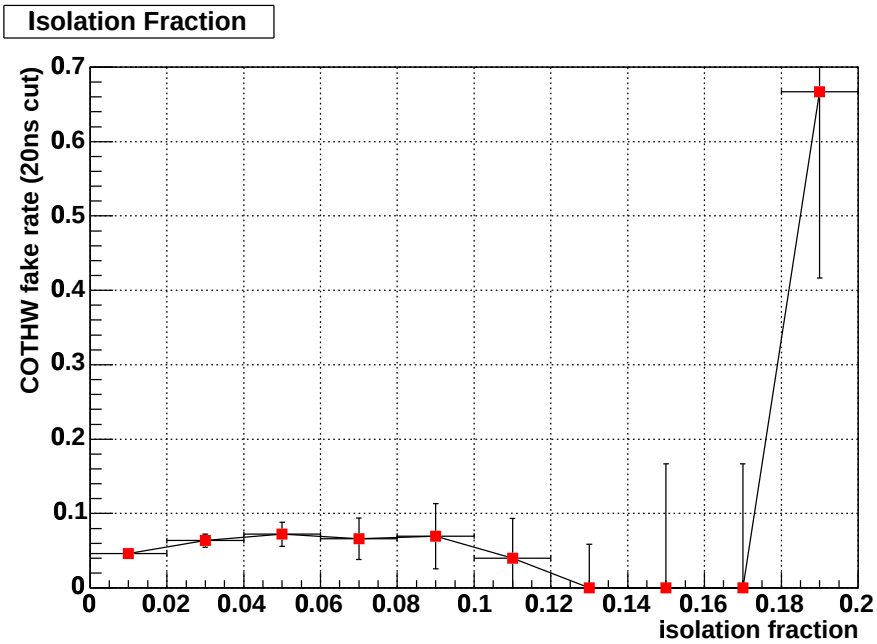

Figure 6.8: Another systematic of $COTHW$ showing a slight upward trend in the fake rate as the region near the track becomes less isolated.

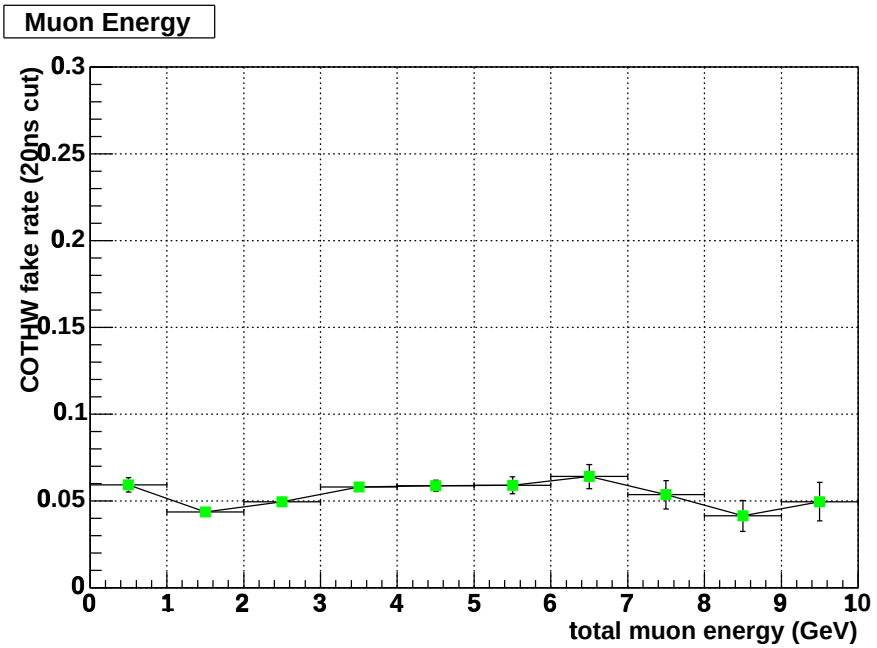

Figure 6.9: Final $COTHW$ systematic plot showing the uncorrelated nature of the tracking dE/dx quantity to the ionization quantities measured by the calorimeter.

The $COTHW$ variable was not properly simulated in electron MC as can be seen in Figure 6.10, so we shifted the $COTHW$ variable in the MC by ~ -10 and smeared it with both a random gaussian and an exponential function to make it look like the electron data. The scaled electron MC $COTHW$ can be seen in Figures 6.11.

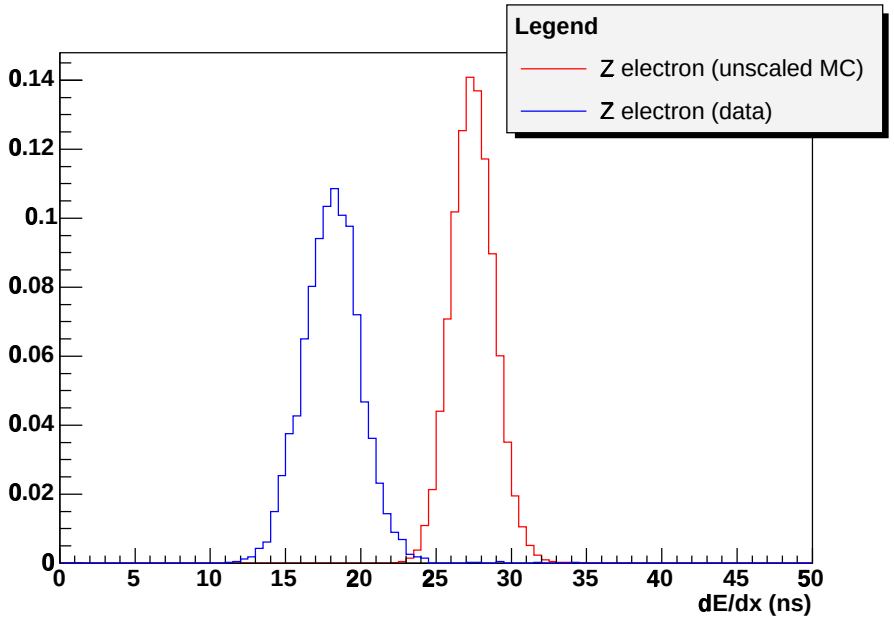

Figure 6.10: The electron Monte-Carlo events clearly have values too large for $COTHW$ and must be shifted.

Table 6.3 shows the $e \rightarrow H^{\pm\pm}$ fake rates we found for both individual and combined ionization variables. Similar to Equation 6.1 in the $\mu \rightarrow H^{\pm\pm}$ fake rate study, the fake rate of the high ionization cuts listed in Table 4.4 and the Stub Cuts in Table 4.2 needed to be factorized for electrons since no events passed all these cuts, for example:

$$\begin{aligned} \text{Net } e \rightarrow H^{\pm\pm} \text{ Tight Muon Fake rate} &= f_3 \times f_4 \times f_5 \\ &= (1.4 \pm 1.4) \times 10^{-9}, \end{aligned} \tag{6.2}$$

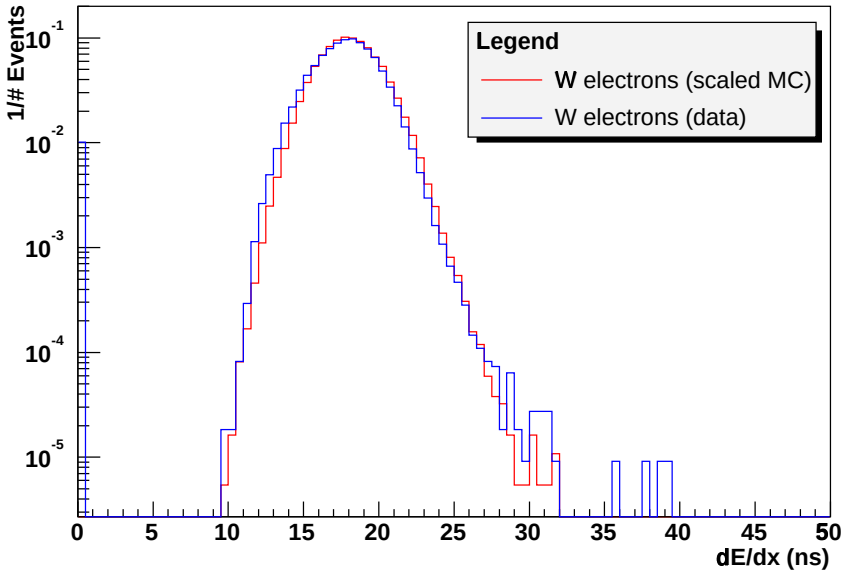

Figure 6.11: After shifting the MC by ~ -10 and smearing with gaussian and exponential random numbers, there is much better agreement with the electron data.

where the factor f_3 comes from the sixth line, f_4 from the eighth, and f_5 from the tenth line in the second portion of Table 6.3. The bottom line $e \rightarrow H^{\pm\pm}$ Tight Muon Fake rate is in the last line of that table and comes from the product of these three factors as shown in Equation 6.2 above.

6.1.4 Measuring $\tau \rightarrow H^{\pm\pm}$ Fake Rates

For the measurement of taus faking doubly charged Higgs, we look at a MC sample of 1 million taus from W in the `wewk4t` dataset. Since muon and electron final products are included in our previous two fake rates, we want this fake rate to include only taus decaying hadronically. We select these hadronic decays by requiring a jet having $E_T > 25$ GeV and $\eta < 1.0$. Only tracks that are reconstructed within $\Delta R < 0.7$ of this primary jet are used, where $\Delta R = \sqrt{\Delta\eta^2 + \Delta\phi^2}$.

Variable(s) cut	Cut value	# Passing	Tight e Track Fake rate (%)
Track	Table 4.2	272,734	
EMET	> 0.6 GeV	264,570	97.01 ± 0.03
HadET	> 4 GeV	6,025	2.21 ± 0.03
EMET & HadET	above	3,352	1.23 ± 0.02
COTHW	> 20 ns	44,500	16.32 ± 0.07
EMET, HadET, & COTHW	above	556	0.204 ± 0.009
COTHW	> 20 ns	44,500	
COTHW	> 35 ns	$0\ (1 \pm 1)$	0.0022 ± 0.0022
Tight Ionization	Tables 4.2 & 4.4	0	$(4.5 \pm 4.5) \times 10^{-6}$

Variable(s) cut	Cut value	# Passing	Tight e Muon Fake rate (%)
Track	Table 4.2	272,734	
EMET	> 0.6 GeV	264,570	97.01 ± 0.03
HadET	> 4 GeV	6,025	2.21 ± 0.03
EMET & HadET	$>$ above	3,352	1.23 ± 0.02
COTHW	> 20 ns	44,500	16.32 ± 0.07
EMET, HadET, & COTHW	above	556	0.204 ± 0.009
EMET & HadET	above	3,352	
Stub	Table 4.2	1	0.030 ± 0.030
COTHW	> 20 ns	44,500	
COTHW	> 35 ns	$0\ (1 \pm 1)$	0.0022 ± 0.0022
Stub & Tight Ion.	Tables 4.2 & 4.4	0	$(1.4 \pm 1.4) \times 10^{-9}$

Table 6.3: *Electron $\rightarrow$ $H^{\pm\pm}$ fake rates with tight ionization cuts.*

Variable(s) cut	Cut value	# Passing	Loose e Track Fake rate (%)
Track	Table 4.2	272,734	
COTHW	> 35 ns	$0\ (1 \pm 1)$	0.00037 ± 0.00037
Loose Ionization	Tables 4.2 & 4.4	0	$(3.7 \pm 3.7) \times 10^{-4}$

Variable(s) cut	Cut value	# Passing	Loose e Muon Fake rate (%)
Track	Table 4.2	272,734	
Stub	Table 4.2	1	$(3.7 \pm 3.7) \times 10^{-4}$
COTHW	> 20 ns	44,500	
COTHW	> 35 ns	$0\ (1 \pm 1)$	0.0022 ± 0.0022
Stub & Loose Ion.	Tables 4.2 & 4.4	0	$(8.2 \pm 8.2) \times 10^{-9}$

Table 6.4: *Electron* $\rightarrow H^{\pm\pm}$ *fake rates with loose ionization cuts.*

We provide two different fake rates from our tau sample. The first is for a hadronic tau faking a highly ionizing track, thus passing all the Track Cuts in Table 4.2 and the three highly ionizing cuts in Table 4.4. The second fake rate is for hadronic taus faking a highly ionizing muon, therefore it must pass the Stub Cuts in Table 4.2 in addition to the cuts made in calculating the previous fake rate. Since no events pass both the Stub Cuts and the high ionization cuts, we factorize this fake rate by requiring these two cut categories separately. Both fake rates are derived in Table 6.5. Since we know from the electron MC that the $COTHW$ variable is not properly modeled in the simulation, we apply the same scaling and smearing corrections to the variable in the tau sample as we show in Figure 6.11.

6.1.5 Measuring QCD $\rightarrow H^{\pm\pm}$ Fake Rates

Our sample of unbiased jets is obtained from QCD data triggered on the `Jet_100` triggers. The mean p_T of this sample is approximately the same as the mean p_T

Variable(s) cut	Cut value	# Passing	Tight Tau Track Fake rate (%)
Hadronic Taus	jet $E_T > 25$, $\eta < 1.0$	61,084	
Track & Tight Ion.	Tables 4.2 & 4.4	0 (1 ± 1)	0.0016 ± 0.0016

Variable(s) cut	Cut value	# Passing	Tight Tau Muon Fake rate (%)
Hadronic Taus	jet $E_T > 25$, $\eta < 1.0$	61,084	
Track & Tight Ion.	Tables 4.2 & 4.4	0 (1 ± 1)	0.0016 ± 0.0016
Track	Table 4.2	4,050	
Track & Stub	Table 4.2	5	0.123 ± 0.055
Track, Stub, & Tight Ion.	Tables 4.2 & 4.4	0	$(2.0 \pm 2.0) \times 10^{-6}$

Table 6.5: $\tau \rightarrow H^{\pm\pm}$ Track and Muon fake rates with tight ionization cuts.

Variable(s) cut	Cut value	# Passing	Loose Tau Track Fake rate (%)
Hadronic Taus	jet $E_T > 25$, $\eta < 1.0$	61,084	
Track & Loose Ion.	Tables 4.2 & 4.4	0 (1 ± 1)	0.0016 ± 0.0016

Variable(s) cut	Cut value	# Passing	Loose Tau Muon Fake rate (%)
Hadronic Taus	jet $E_T > 25$, $\eta < 1.0$	61,084	
Track & Loose Ion.	Tables 4.2 & 4.4	0 (1 ± 1)	0.0016 ± 0.0016
Track	Table 4.2	4,050	
Track & Stub	Table 4.2	5	0.123 ± 0.055
Track, Stub, & Loose Ion.	Tables 4.2 & 4.4	0	$(2.0 \pm 2.0) \times 10^{-6}$

Table 6.6: $\tau \rightarrow H^{\pm\pm}$ Track and Muon fake rates with loose ionization cuts.

for the stable $H^{\pm\pm}$. We make the assumption that the maximum E_T jet is the one responsible for firing the jet trigger. We have compared fake rates for tracks having $\Delta R > 0.7$ of the primary jet to those inside that cone, where $\Delta R = \sqrt{\Delta\eta^2 + \Delta\phi^2}$. We combine the two samples for calculating our fake rates and provide systematic errors to cover the differences we find in the fake rates when calculating inside-jet and outside-jet separately.

We select a base track sample that pass the cuts in Table 6.7. We then check for highly-ionizing events in this sample by counting the number of tracks which pass both the Track Cuts in Table 4.2 and the highly ionizing cuts in Table 4.4. We perform a similar process to find the QCD *Muon* fake rate by counting the number of tracks in the jet samples which pass our base muon cuts in Table 6.7 and the number passing the $H^{\pm\pm}$ ID cuts in Table 4.4. These fake rates and the numbers used to find them are all found in Table 6.9.

We also looked for a p_T dependence in our track fake rate using loose ionization cuts. This was the only sample with high enough statistics for a potentially meaningful result. Table 6.8 shows the fake rates for tracks having p_T greater than or less than 40 GeV (the mean of the momentum distribution), as well as for tracks inside or outside the primary jet (an inside jet track is defined as having $\Delta R < 0.7$ from the highest E_T jet in the event). The high p_T tracks have a larger fake rate both inside and outside the leading jet. Since the mean of the $H^{\pm\pm}$ p_T distribution is in the 40 GeV range, we apply no p_T dependent fake rates. We show systematic errors which cover the differences in fake rates for particles whose p_T lies above 40 GeV or whose p_T lies below 40 GeV.

A confirmation of the overestimate of the QCD Muon fake rate using jet data came through the analysis of a control sample within the muon data. We currently

Variable	Cut
Base Track	
ΔR from primary jet	> 0.7
$\lvert z_0 \rvert$	< 60.0 cm
# Stereo hits	≥ 3 SL with ≥ 5 hits or COT layer < 96
# Axial hits	≥ 3 SL with ≥ 5 hits or COT layer < 96
$\lvert d_0 \rvert$	< 0.2 cm
(isolation in R=0.4 cone)/p_T	< 1.0
p_T	> 20 GeV
ρ_{COT}	> 140 cm
Cosmic Ray Veto	
Base Muon	
All Base Track cuts	(see above)
$\lvert \Delta x_{CMU} \rvert$	< 3.0 cm
$\lvert \Delta x_{CMP} \rvert$	< 5.0 cm
$\lvert \Delta x_{CMX} \rvert$	< 6.0 cm

Table 6.7: Base Track and Base Muon Cuts used in calculating the QCD fake rates.

Track selection	# Tracks passing Loose ionization cuts	# of Base tracks	Fake rate (%)
$p_T < 40$ GeV Inside jet	6	188,172	0.00319 ± 0.00130
$p_T < 40$ GeV Outside jet	85	159,401	0.0533 ± 0.0058
$p_T > 40$ GeV Inside jet	31	191,606	0.0162 ± 0.0029
$p_T > 40$ GeV Outside jet	82	100,151	0.0819 ± 0.0090

Table 6.8: Loose QCD Track $\rightarrow H^{\pm\pm}$ fake rates in bins of inside/outside jet and high/low p_T.

Variable(s) cut	Cut value	# Passing	Tight QCD Track Fake rate (%)
Base Track	Table 6.7	639,330	
Track & Tight Ion.	Tables 4.2 & 4.4	18	$0.00282 \pm 0.00066(stat)$ $^{+0.00034}_{-0.00051}(syst)$

Variable(s) cut	Cut value	# Passing	Tight QCD Muon Fake rate (%)
Base Muon	Table 6.7	5,416	
Track & Stub	Table 4.2	354	6.54 ± 0.34
EMET	> 0.6 GeV	94	1.74 ± 0.18
HadET	> 4 GeV	69	1.27 ± 0.15
EMET, HadET	above	46	0.849 ± 0.125
EMET, HadET, COTHW	above, > 20 ns	12	0.222 ± 0.064
COTHW	> 35 ns	1	1.82 ± 1.80
Track, Stub, & Tight Ion.	Tables 4.2 & 4.4	1	0.0185 ± 0.0185

Table 6.9: QCD $\rightarrow H^{\pm\pm}$ Track and Muon fake rates with tight ionization cuts. The Track fake rate includes systematic errors to cover the range between the fake rates for samples both inside and outside the primary jet. The statistics are too low to include systematic errors for p_T dependence as well.

Variable(s) cut	Cut value	# Passing	Loose QCD Track Fake rate (%)
Base Track	Table 6.7	639,330	
Track & Loose Ion.	Tables 4.2 & 4.4	204	$0.0319 \pm 0.0022(stat)$ $^{+0.0500}_{-0.0287}(syst)$

Variable(s) cut	Cut value	# Passing	Loose QCD Muon Fake rate (%)
Base Muon	Table 6.7	5,416	
Track & Stub	Table 4.2	354	6.54 ± 0.34
COTHW	> 35 ns	1	0.0185 ± 0.0185
Track, Stub, & Loose Ion.	Tables 4.2 & 4.4	1	0.0185 ± 0.0185

Table 6.10: QCD $\rightarrow H^{\pm\pm}$ Track and Muon fake rates with loose ionization cuts. The Track fake rate includes systematic errors to cover the range between the fake rates for $p_T > 40$ GeV and $p_T < 40$ GeV samples for both inside and outside the primary jet.

wish to preserve the blind status of the topology containing a single highly-ionizing track with stub and high $\not\!\!E_T$, so we looked in the data for single track events passing our Track, Stub, and Ionization cuts having $\not\!\!E_T < 20$ GeV. We found 0 such events using our tight ionization cuts and also 0 events using our loose cuts. Using our fake rates from the jet sample calculated above, we would have expected many QCD events to populate this sample. The absence of such events shows that our factorized QCD Muon fake rates are overestimates. Therefore, in order to better pin down these fake rates, we will use this muon control sample for QCD Muon fake rate calculations. For the denominator of this fake rate, we counted the number of events in the muon data having only a "base muon" (with no additional base tracks) and $\not\!\!E_T < 20$ GeV. Table 6.11 shows the numbers we obtained to calculate this fake rate.

Variable(s) cut	Cut value	# Passing	QCD Muon Fake rate (%)
Single Base Muon	Table 6.7, $\not\!\!E_T < 20GeV$	213,102	
Track, Stub, & Ion.	Tables 4.2 & 4.4	0 (1 ± 1)	0.000469 ± 0.000469

Table 6.11: QCD $\rightarrow H^{\pm\pm}$ Muon fake rates measured from a low $\not\!\!E_T$, single-track muon sample. This single fake rate is the same using both loose and tight ionization cuts, so we only give it once here. This fake rate, coupled with the QCD Track (loose and tight) fake rates from the jet samples is used in calculating the QCD background.

6.2 Backgrounds

One advantage of performing a search for a long-lived doubly-charged particle is the lack of SM background. We expect the background to come in the form of highly ionizing muons, electrons, hadronic taus, and QCD jets as described in Section 6.1 above.

6.2.1 Muon Background

It is possible for a Z event to produce these highly ionizing muons which make up the background for our study. Table 6.12 shows the expected number of muon background events. The background from muons would be proportional to the square of the muon fake rate (accounting for the duplicity of muons present, both of which must be fakes). Since cosmics are muon events and may be contained in this data sample, the background due to cosmics is also covered by this calculation.

	Loose Search	Tight Search
# $Z \to \mu\mu$ events	10,457	10,457
(μ Fake rate)^2	$(3.1 \pm 3.1 \pm 0.6) \times 10^{-11}$	$(3.2 \pm 3.2 \pm 0.5) \times 10^{-16}$
# μ Bkg. events	$(3.2 \pm 3.2 \pm 0.6) \times 10^{-7}$	$(3.3 \pm 3.3 \pm 0.5) \times 10^{-12}$

Table 6.12: Long-lived doubly-charged Higgs background due to highly ionizing muons from Z's. The first uncertainties are all statistical and the second are systematic.

6.2.2 Electron Background

It is also plausible for a Z event to produce electrons which are highly ionizing in both the tracking chamber and the calorimeters. Such an event would not only have to deposit a portion of it's energy in the electromagnetic calorimeter, but it would also need to slip through a crack in the detector and deposit energy in the hadronic calorimeter as well. The background calculation from electrons we present here employs the product of the $e \to H^{\pm\pm}$ Muon and Track fake rate which we measured using $Z \to ee$ Monte-Carlo in Section 6.1.3. Both the Muon and Track versions of this fake rate must be incorporated since one of the electrons would be required to have a stub in order to fake a $H^{\pm\pm}$, with the other one having only a highly ionizing track. We rely on the correct modeling of the detector cracks in the simulation to give us an accurate background measurement.

In order to estimate the number of $Z \to ee$ background events, we perform a calculation as follows:

$$\begin{aligned} Z \to ee \text{ background} &= \left(n_1 \left(\frac{n_2}{n_3} \right) \left(\frac{\mathcal{L}_\mu}{\mathcal{L}_e} \right) \right) \times e_{Trk} \times e_{Mu} \\ &= \left(\text{Est.\# } Z \to ee \text{ fakable events} \right) \times e_{Trk} \times e_{Mu}, \end{aligned} \quad (6.3)$$

where n_1 is the number of events in the $Z \rightarrow ee$ MC that passed the Track Cuts[1], n_2 and n_3 are the number of Z candidates in electron data and Z MC samples respectively, and $\mathcal{L}_\mu$ and $\mathcal{L}_e$ are the integrated luminosities of the respective data samples. In addition, e_{Trk} gives the fake rate for an electron faking a highly ionizing track and e_{Mu} gives the fake rate for an electron faking a highly ionizing track with a stub.

Table 6.13 shows the values for these variables, and Table 6.14 shows the Z electron backgrounds derived using this method.

n_1	n_2	n_3	$\mathcal{L}_\mu$	$\mathcal{L}_e$
95,435	3,158	20,691	292.0 pb^{-1}	264.0 pb^{-1}

Table 6.13: Values in Equation 6.3 that are used in calculating the estimated number of fakable electron events in the μ data sample.

	Loose Search	Tight Search
Est.# $Z \rightarrow ee$ events	16,111	16,111
e (Muon $\times$ Track) Fake rate	$(3.0 \pm 3.0) \times 10^{-16}$	$(6.3 \pm 6.3) \times 10^{-19}$
# e Background events	$(4.8 \pm 4.8) \times 10^{-12}$	$(1.0 \pm 1.0) \times 10^{-14}$

Table 6.14: Long-lived doubly-charged Higgs background due to highly ionizing electrons from Z's.

6.2.3 Tau Background

A tau decaying hadronically could in theory have high enough ionization in the detector to pass the doubly charged Higgs ionization cuts and also punch through

[1]This is a separate MC sample (480,000 events from the `zewk1e` dataset) than that used for finding the electron fake rate in Table 6.3.

into the muon chamber. We calculate the background we should expect from this type of event using the tau fake rates we measured in Section 6.1.4.

We estimate the number of fakable tau events based on the number of $Z \to \mu\mu$ events we count in the data. Since this number can be corrected up based on muon inefficiency and down due to hadronic tau branching for the two τ's per event, we apply the following corrections to derive an estimated number of $Z \to \tau\tau$ events in the data:

$$\begin{aligned} \text{Est.\# } Z \to \tau\tau\text{'s} &= N_{\mu\mu} \times \left(\frac{1}{\epsilon_{\mu\mu}}\right) \times \tau_{\text{B.R.}} \\ &= 10,457 \times \left(\frac{1}{0.832 \times 0.968}\right) \times 0.876 \\ &= 11,374 \text{ events}, \end{aligned} \tag{6.4}$$

where $N_{\mu\mu}$ gives the number of $Z \to \mu\mu$ events counted, $\epsilon_{\mu\mu}$ gives the measured $Z \to \mu\mu$ efficiency, and $\tau_{B.R.}$ gives the branching ratio of ≥ 1 hadronic tau. The backgrounds can be calculated directly from this estimated number of events, provided the fake rate applied is the product of the τ Track and Muon fake rates, since both a track and a stub are required in the search. These tau backgrounds are shown in Table 6.15.

	Loose Search	Tight Search
Est.# $Z \to \tau\tau$ events	11,374	11,374
τ (Muon $\times$ Track) Fake rate	$(3.2 \pm 3.2) \times 10^{-13}$	$(3.2 \pm 3.2) \times 10^{-13}$
# τ Background events	$(3.6 \pm 3.6 \times 10^{-9}$	$(3.6 \pm 3.6) \times 10^{-9}$

Table 6.15: Long-lived doubly-charged Higgs background due to highly ionizing hadronic taus from Z's.

6.2.4 QCD Background

We consider the case where unbiased jet events are misidentified as highly ionizing particles. We use the QCD Track and QCD Muon fake rates measured in Section 6.1.5. Recall that the we use the QCD Muon rates measured from the low-$\not\!\!E_T$ muon sample and the QCD Track rates from jet samples.

In order to find the QCD background contribution, we count the number of fakable QCD events using basic criteria. Fakable QCD events are defined as those events in our muon sample having both a base track and base muon (from Table 6.7). The number of background events from QCD can then be calculated by multiplying the number of fakable events by the product of the QCD Muon and QCD Track fake rates. The results of these QCD background calculations are shown in Table 6.16.

	Loose Search	Tight Search
# fakable QCD events	19,198	19,198
QCD (Muon × Track) Fake rate	$(1.5 \pm 1.5^{+2.4}_{-1.3}) \times 10^{-9}$	$(1.3 \pm 1.3^{+0.2}_{-0.2}) \times 10^{-10}$
# QCD Background events	$(2.9 \pm 2.9^{+4.5}_{-2.6}) \times 10^{-5}$	$(2.5 \pm 2.5 \pm 0.4) \times 10^{-6}$

Table 6.16: Long-lived doubly-charged Higgs background due to QCD. The first set of uncertainties on the measurements are statistical and the second are systematic.

6.2.5 Total Background

The net background is found by adding the highly ionizing muon, electron, tau, and QCD backgrounds. Table 6.17 shows this calculation of the total background expected in the data for quasi-stable doubly-charged Higgs events. Having an expected background so much smaller than one is a rarity for an exotic search of this type. As a result, we anticipate that any observed events within the search region

are highly likely to be signal.

Background source	# Background Events in Loose Search	# Background Events in Tight Search
$Z \to \mu\mu$	$< 10^{-6}$	$< 10^{-11}$
$Z \to ee$	$< 10^{-11}$	$< 10^{-13}$
$Z \to \tau\tau$	$< 10^{-8}$	$< 10^{-8}$
QCD	$(2.9 \pm 2.9^{+4.5}_{-2.6}) \times 10^{-5}$	$(2.5 \pm 2.5 \pm 0.4) \times 10^{-6}$
All combined	$(2.9 \pm 2.9^{+4.5}_{-2.6}) \times 10^{-5}$	$(2.5 \pm 2.5 \pm 0.4) \times 10^{-6}$

Table 6.17: Total background in both loose and tight search topologies from all potential sources for quasi-stable doubly-charged Higgs.

Chapter 7

Results

We observe no doubly-charged two-track events passing either the loose or tight ionization cuts. We use this lack of evidence for stable doubly-charged particles to set limits on long-lived doubly-charged Higgs pair production.

To set a limit on the mass of the $H^{\pm\pm}$ we have chosen *apriori* to use our loose ionization cuts to determine the experimental cross section. We use a Bayesian approach for this process [21]. After entering the total background expected for our signal, the error on that background, and a 16.8% error on the acceptance (mean value for the four mass points), the "bayes.f" program (provided by the CDF Statistics Group) returned a value of < 3.247 signal events at a 95% C.L. for 0 events observed. This permitted us to find the experimental cross section for each doubly-charged Higgs mass when put into the following equation:

$$\begin{aligned} \sigma_{exp}(M_H) &= \frac{\#\text{ signal events}}{luminosity \times \text{“}Loose\ Acc \times Eff''(M_H)} \\ &= \frac{3.247}{(292.0 \pm 16.6)\, pb^{-1} \times \text{“}Loose\ Acc \times Eff''(M_H)}. \end{aligned} \tag{7.1}$$

From this equation we received four experimental cross-section limits for Higgs masses of 90, 100, 130, and 160 GeV shown in Table 7.1. Since we expected only negligible background, our *apriori* expected limit plot is identical to the limit plot

from the data. The data result in a lower mass limit of 146 GeV for long-lived $H^{\pm\pm}$ in all decay channels. The systematic errors are taken by adding in quadrature all relative experimental errors in Table 5.9 (K factor and PDF cross section errors are applied to theoretical cross section so were not included here) and applying the total relative error to the calculated cross section. We use the next to leading order theoretical cross sections at each respective mass [20].

$H^{\pm\pm}$ mass	Loose Acc×Eff	Experimental σ (pb)	Theoretical σ_{NLO} (pb)
90 GeV	$0.280 \pm .035$	$0.0397 \pm .0055 \pm .0054$	$0.26443 \pm .02311$
100 GeV	$0.288 \pm .036$	$0.0386 \pm .0053 \pm .0053$	$0.17435 \pm .01553$
130 GeV	$0.316 \pm .040$	$0.0352 \pm .0049 \pm .0048$	$0.05783 \pm .00523$
160 GeV	$0.341 \pm .043$	$0.0326 \pm .0045 \pm .0045$	$0.02186 \pm .00204$

Table 7.1: Cross section limits for long-lived doubly-charged Higgs at the mass values of 90, 100, 130, and 160 GeV. The listed errors are statistical, except for the second error for experimental σ and the errors on the theoretical σ_{NLO}.

Figure 7.1 illustrates the mass limit set by this analysis by showing where the curves created by our theoretical and experimental cross sections intersect.

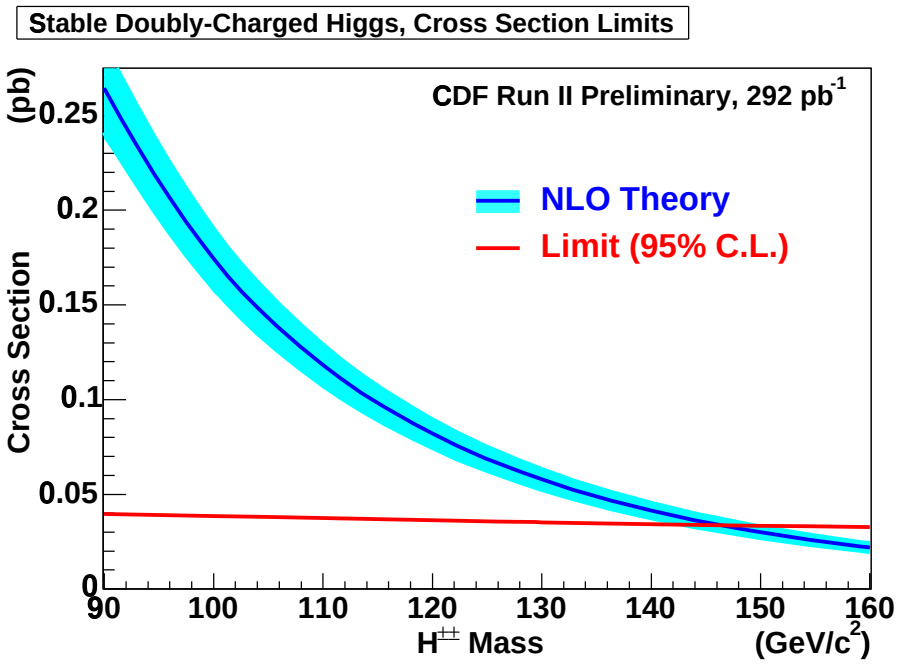

Figure 7.1: The theoretical and experimental $H^{\pm\pm}$ cross section limits for the loose ionization cuts. The intersection corresponds to a long-lived doubly-charged Higgs mass limit for the analysis of 146 GeV.

Chapter 8

Conclusions

In summary, we have analyzed nearly 300 pb^{-1} of high-p_T collision data from CDF in search for long-lived doubly-charged Higgs bosons. Based on these particles' signatures of muon-like penetration in the detector and high ionization, we were able to define a search region where the Higgs should be detectable. Using a combination of detector data collected outside the search region and Monte Carlo simulated particles, the analysis was determined to have extremely low background levels. As a result, any particle pair passing the Higgs selection cuts would be a strong candidate for a pair of doubly-charged Higgs particles.

Having not found any such particle pairs passing the selection cuts, this analysis produced no $H^{\pm\pm}$ candidates. We use this knowledge along with the theoretical cross-section to set a lower bound of 146 GeV at the 95% confidence level on the mass of pair-produced $H^{\pm\pm}$ in the context of left-right symmetric models. Thus, our search improves on all previous mass limits by nearly 50 GeV [22, 23].

Bibliography

[1] C. Hays and A. Kotwal, *CDF Note* **6342** (2003).

[2] C. Hays and A. Kotwal, *CDF Note* **6457** (2003).

[3] C. Hays and A. Kotwal, *CDF Note* **6604** (2003).

[4] J. Tuttle *et al. CDF Note 6856* (2004).

[5] J. Tuttle *et al. CDF Note 7050* (2004).

[6] M. H. Ahn *et al. Phys. Rev. Lett.,* **90** ,041801 (2003).

[7] R. Mohapatra and G. Senjanovic, *Phys. Rev. Lett.,* **44** ,912 (1980).

[8] J. F. Gunion *et al. Phys. Rev. D,* **40** ,1546 (1989).

[9] Z. Chacko and R. N. Mohapatra, *Phys. Rev. D,* **58** ,015003 (1998).

[10] M. Frank, *Phys. Rev. D,* **63** ,034009 (2001).

[11] D. E. Groom *et al. Eur. Phys. J.,* **C15** ,1 (2000).

[12] S. Yu *et al. CDF Note* **6361** (2003).

[13] G. Punzi, D. Tonelli, *et al. CDF Note* **6932** (2004).

[14] H. Gerberich *et al. CDF Note* **6089** (2002).

[15] C. Hays and A. Kotwal, *CDF Note* **6833** (2004).

[16] W. Orejudos and F.D. Snyder, *CDF Note* **6307** ver.2.1 (2003).

[17] D. Amidei *et al. CDF Note* **6711** ver.3 (2003).

[18] S. Klimenko *et al. CDF Note* **6314** (2004).

[19] The EWK prescription for determining PDF uncertainty can be found in this talk: http://www-cdf.fnal.gov/internal/WebTalks/0404/links/040402_joint_physics_Tony_1_JointPhys_040204.pdf.

[20] M. Muhlleitner and M. Spira, *Phys. Rev. D.,* **68** ,117701 (2003).

[21] The Fortran code from the CDF Statistics group for calculating the Bayesian probability can be found at http://www-cdf-fnal.gov/physics/statistics/code/bayes.f.

[22] DELPHI Collaboration, *Phys. Lett. B.,* **552** ,127 (2003).

[23] OPAL Collaboration, *Phys. Lett. B.,* **526** ,221 (2002).